Tumor-stroma mechanics coordinate amino acid availability to sustain tumor growth and malignancy

Thomas Bertero, William M. Oldham, Eloise M. Grasset, Isabelle Bourget, Etienne Boulter, Sabrina Pisano, Paul Hofman, Floriant Bellvert, Guerrino Meneguzzi, Dmitry V. Bulavin, et al.

Version of Record: https://www.sciencedirect.com/science/article/pii/S1550413118305771
Manuscript_2fe2e57da69107f35d7b415c8315e853

Tumor-stroma mechanics coordinate amino acid availability to sustain tumor growth and malignancy

Thomas Bertero[1*§], William M. Oldham[2], Eloise M. Grasset[1], Isabelle Bourget[1], Etienne Boulter[1], Sabrina Pisano[1], Paul Hofman[1,3], Floriant Bellvert[4,5], Guerrino Meneguzzi[1], Dmitry V. Bulavin[6], Soline Estrach[1], Chloe C. Feral[1], Stephen Y. Chan[7] , Alexandre Bozec[1,8] and Cedric Gaggioli[1*].

(1) University Côte d'Azur, CNRS UMR7284, INSERM U1081, Institute for Research on Cancer and Aging, Nice (IRCAN), Nice, France.
(2) Division of Pulmonary and Critical Care Medicine, Department of Medicine, Brigham and Women's Hospital, Harvard Medical School, Boston, MA, 02115, USA;
(3) University Côte d'Azur, Laboratory of Clinical and Experimental Pathology, Biobank 0033-00025 and FHU OncoAge, Pasteur Hospital, Nice, France.
(4) LISBP, Université de Toulouse, CNRS, INRA, INSA, Toulouse, France.
(5) MetaToul-MetaboHUB, National infrastructure of metabolomics and Fluxomics, Toulouse, France
(6) University Côte d'Azur, CNRS UMR7284, INSERM U1081, Institute for Research on Cancer and Aging, Nice (IRCAN), Centre Antoine Lacassagne, Nice, France.
(7) Center for Pulmonary Vascular Biology and Medicine, Pittsburgh Heart, Lung, Blood, and Vascular Medicine Institute, Division of Cardiology, Department of Medicine, University of Pittsburgh Medical Center, Pittsburgh, PA, 15261, USA;
(8) Face and Neck University Institute Department of Oncologic Surgery, Nice,, France,

[§] **Leading contact**: Thomas Bertero, PhD

[*]**Corresponding Authors**:
Cedric Gaggioli, PhD
Université Côte d'Azur
Institute for Research on Cancer and Aging, Nice
INSERM, U1081, CNRS, UMR7284
28 Av de Valombrose 06107 Nice Cedex 02, France
Tel :+33 (0)4 93 37 76 93
Fax : :+33 (0)4 93 37 76 76
Email : gaggioli@unice.fr

and

Thomas Bertero, PhD
Université Côte d'Azur
Institute for Research on Cancer and Aging, Nice
INSERM, U1081, CNRS, UMR7284
28 Av de Valombrose 06107 Nice Cedex 02, France
Tel :+33 (0)4 93 37 77 53
Fax : :+33 (0)4 93 37 76 76
Email : bertero@unice.fr

Summary

Dysregulation of extracellular matrix (ECM) deposition and cellular metabolism promotes tumor aggressiveness by sustaining the activity of key growth, invasion, and survival pathways. Yet, mechanisms by which biophysical properties of ECM relate to metabolic processes and tumor progression remain undefined. In both cancer cells and carcinoma-associated fibroblasts (CAF), we found that ECM stiffening mechanoactivates glycolysis and glutamine metabolism and thus coordinates non-essential amino acid flux within the tumor niche. Specifically, we demonstrate a metabolic crosstalk between CAF and cancer cells in which CAF-derived aspartate sustains cancer cell proliferation, while cancer cell-derived glutamate balances the redox state of CAF to promote ECM remodeling. Collectively, our findings link mechanical stimuli to dysregulated tumor metabolism and thereby highlight a new metabolic network within tumors in which diverse fuel sources are used to promote growth and aggressiveness. Furthermore, this study identifies potential metabolic drug targets for therapeutic development in cancer.

Introduction

Non-transformed cells within the tumor microenvironment continuously co-evolve with tumor cells to promote tumorigenesis (Kalluri, 2016; Quail and Joyce, 2013). To promote tumorigenesis, normal fibroblasts interact with tumor cells and are converted to Carcinoma-Associated Fibroblasts (CAF). CAF promote extensive tissue remodeling (or tumor niche formation). Further establishment of a complex, dynamic network of cytokines, chemokines, growth factors, and matrix remodeling enzymes ultimately changes the physical and chemical properties of the tumor (Pickup et al., 2014). Indeed, tumors exhibit altered tissue-level and cell mechanics (Kai et al., 2016). Experimental models demonstrate that enhancing ECM stiffness promotes malignancy, and, conversely, inhibiting matrix stiffening reduces tumor incidence (Levental et al., 2009). While genetic modifications in tumor cells undoubtedly initiate and drive malignancy (Watson et al., 2013), cancers progresse within a dynamically evolving ECM that modulates virtually every behavioral facet of tumor cells, including sustained proliferation, evasion of growth suppression, death resistance, induced angiogenesis and initiation of invasion (Pickup et al., 2014). Nevertheless, the processes that link ECM mechanotransduction (i.e., the processes that enable cells to sense and adapt to external mechanical forces) to the molecular mechanisms that influence cell behavior and modulate malignancy are just beginning to be defined.

Tumors alter their metabolic program to maintain cell autonomous proliferation, even in the nutrient-poor conditions of the tumor microenvironment (Vander Heiden and DeBerardinis, 2017). Some of the most striking changes of tumor cellular bioenergetics include Warburg metabolism (i.e., a chronic shift in energy production from mitochondrial oxidative phosphorylation to glycolysis) and increases in glutaminolysis, amino acid and lipid metabolism, flux through the pentose phosphate pathway, macromolecule biosynthesis, and mitochondrial biogenesis, as well as maintenance of the redox state (Ben-Sahra and Manning, 2017; Vander Heiden and DeBerardinis, 2017). Prior mechanistic studies in cancer utilized hypoxia exposure to investigate this metabolic shift. Yet, numerous tumors are also

characterized by profound metabolic dysregulation in the absence of obvious hypoxic stress (Hensley et al., 2016). Data are emerging regarding the molecular regulators of metabolic dysfunction operating independently of outright hypoxic stress. While extracellular protein can provide nutrients to the starved cancer cells (Davidson et al., 2017), we hypothesized that mechanical stimuli from the tumor niche provide additional molecular signals to guide tumor cells in capturing nutrients to support their metabolic needs.

Two related transcriptional coactivators inherent to the Hippo signaling pathway, Yes-associated protein 1 (YAP) and TAZ (or WWRT1), are mechanoactivated by stiff ECM and function as central regulators of cellular proliferation, survival and polarity particularly in development and cancer progression (Dupont et al., 2011; Yu et al., 2015). Increasing evidences suggest a central connection of mechanotransduction – including the YAP/TAZ pathway – with cellular metabolism (Santinon et al., 2018; Yang et al., 2018), and processes related to glucose consumption and Warburg metabolism (Bays et al., 2017; Enzo et al., 2015; Mo et al., 2015; Sorrentino et al., 2014; Wang et al., 2015). However, increased glycolysis alone is insufficient to meet the total metabolic demands of proliferating cells. A less appreciated aspect of cancer cell metabolism is the need to rewire carbon and nitrogen flux to generate the building blocks required for rapid cell growth. The tricarboxylic acid (TCA) cycle also serves as a source of precursors to provide lipids to generate membranes, amino acids for macromolecules and proteins, and nucleotides for DNA and RNA synthesis, particularly in rapidly growing tissues (Vander Heiden and DeBerardinis, 2017). Continued functioning of the TCA cycle requires the replenishment of carbon intermediates, know as anaplerosis; (Vander Heiden and DeBerardinis, 2017)). Glutaminolysis (glutamine catabolism to generate TCA cycle intermediates) via glutaminase (GLS1) is among the best-described anaplerotic pathways in cancer cells (Hensley et al., 2013). The ability of glutaminolysis to support Aspartate (Asp) production for direct induction of proliferation has recently been reported in malignant cells (Birsoy et al., 2015; Sullivan et al., 2015). Furthermore, exchange of amino acids between cells within the tumor has recently been proposed as an alternative

avenue of metabolic support for the tumor (Sousa et al., 2016; Yang et al., 2016). The CAF is a predominant cell type in the squamous cell carcinoma (SCC) stroma and an important mediator of the desmoplastic response (Quail and Joyce, 2013) which results in increased tumor niche stiffness. Consequently, in this study we investigated whether a metabolic response to tumor niche stiffness controls tumor progression. Specifically, we aimed to determine whether ECM stiffness directly modulates both cancer cell and CAF metabolism and coordinates nutrient availability within the tumor niche to support the metabolic needs of tumor progression. Such a hypothesis would effectively link tumor niche stiffness and metabolic dysfunction as two integrally related molecular drivers of cancer.

Results

Mechanical stimuli regulate metabolic reprogramming and coordinate non-essential amino acid exchange within the tumor niche.

ECM stiffness activates carcinoma cells (CC) and CAF pro-tumoral activities (Pickup et al., 2014). In order to sustain these energy-requiring activities, cells adapt their metabolism accordingly (Vander Heiden and DeBerardinis, 2017). To determine whether mechanical/physical cues conveyed by ECM stiffness modulate CC and CAF metabolism, we performed a series of metabolomic studies in CC and CAF cultivated on physiological (soft; 1kPa) or pathophysiological (stiff; 8kPa) ECM (**Fig.1 and Fig.S1-2**). In the first instance, we investigated changes in oxygen consumption rate (OCR) and extracellular media acidification rate (ECAR), measures of mitochondrial activity and glycolysis, respectively. While, in CCs, glycolysis is increased upon stiffness, mitochondrial activity showed minimal changes (**Fig.1A**). By contrast in CAFs, both mitochondrial activity and glycolysis were significantly increased by stiffness (**Fig.1E**). Consistent with increased glycolysis in stiff condition, we observed an increase of glucose consumption (**Fig.S1A,J**) and lactate secretion (**Fig.S1B,K**) in these cells. Importantly, a decrease of TCA cycle intermediates was observed in CCs (**Fig.S1C**), while in CAFs, an increase of TCA cycle intermediates was observed (**Fig.S1L**), consistent with the extracellular flux analyses that suggested increased oxidative phosophorylation in CAFs on stiff ECM. U-$^{13}C_6$-glucose tracing experiments in CCs (**Fig.1B**) and CAFs (**Fig.1F**) confirmed that glycolysis is activated upon exposure to stiff matrix. Thus, matrix stiffening reprograms glucose metabolism in tumor cells.

As aerobic glycolysis alone is insufficient to meet the metabolic needs of proliferating cells, we hypothesized that ECM stiffening also reprogrammed amino acid metabolism. Accordingly, we performed kinetic studies and found that both CCs (**Fig.1C** and **Fig.S1D**) and CAFs (**Fig.1G** and **Fig.S1M**) increased glutamine (Gln) consumption in stiff matrix. Consistent with increased glycolysis and Gln metabolism, we observed an increase in

transcript levels, protein levels, and enzyme activity of Gln metabolism-related genes (**Fig.S1E-I** and **Fig.S1N-R**). In addition, our kinetic studies revealed that glutamate (Glu) was secreted and Asp was taken up by CCs (**Fig.S1D**); while in CAFs, Asp was secreted, and Glu was taken up (**Fig.S1M**). In the context of tumor cells *in vivo*, the more important parameters to assess include the release and uptake rates of Asp/ Glu relative to each other. As such, We found that upon exposure to stiff matrix, the secreted levels of Asp/Glu were similar to the levels of Asp/Glu taken up by the cells (**Fig.1D,H**), suggesting a possible crosstalk within the microenvironment.

To confirm a metabolic crosstalk between CCs and CAFs, we performed a series of metabolomic and functional studies. Specifically, we sought to identify molecules that were over-represented in CAF medium (and therefore secreted by CAFs); under-represented in the CAF medium after contact with CCs (removed by CCs); and over-represented inside CCs treated with the CAF medium (taken up by CCs; **Fig.1I**). Based on our previous results (**Fig.1D,H**) that identified complementary secretion and uptake of Asp and Glu between CAFs and CCs, we focused specifically on amino acids. We found that Asp was secreted by CAFs and appeared to be taken up by CCs (**Fig.1J** and **Fig.S2A**). Moreover, we found that Glu is increased in CC medium, decreased in the CC medium after contact with CAF cells, and increased inside CAFs treated with the CC medium (**Fig.1K** and **Fig.S2B-D**). Thus, these results indicate that metabolic crosstalk between CCs and CAFs may rely upon dynamic alterations of amino acid flux. To test whether such metabolic crosstalk is able to sustain pro-tumoral behavior activated by matrix stiffening, we assessed changes in cell proliferation (**Fig.1L-M**) and cell contractility (**Fig.1N-O**), in CCs and CAFs, respectively. CCs showed an increase of proliferation when cells were treated with media containing Asp (**Fig.1L**) or with CAF-conditioned medium (CAF-CM), a feature that was dependent on matrix stiffness during the conditioning process (**Fig.S1S**) and was reproducible with multiple primary specimens (**Fig.S1T-U**). Notably, CAF-CM retained the ability to increase CC proliferation even if the CAF-CM was subjected to three freeze-thaw cycles (- 80 °C, 60 °C;

Fig.S1S) or heating (100 °C, 15 min; **Fig.1L** and **Fig.S1T-U**), indicating that the factor(s) lacked tertiary structure and could be a metabolite. Treatment of CCs with Asp had the ability to increase CC proliferation to a degree comparable to that of CAF-CM (**Fig.1L** and **Fig.S1S-U**). Conversely, the CAF ability to generate contractile forces was increased when cells were treated with media supplemented with Glu (**Fig.1N**) or with CC-conditioned medium (SCC12-CM; **Fig1M**), a feature that was also dependent upon matrix stiffness during the conditioning process (**Fig.S1V**) and was reproducible with multiple cancer cell lines (**Fig.S1W-X**). As with CAFs, CC-CM retained the ability to increase CAF contractility even after freeze-thaw (**Fig.S1V)** or heating (**Fig.1M** and **Fig.S1V-X**). Treatment of CAF with Glu had the ability to increase CAF contractility to a degree comparable to that of CC-CM (**Fig.1M and Fig.S1V-X**). Taken together, stiff matrices sustain the metabolic demands of tumor microenvironment cells by activating glycolysis and Gln metabolism and coordinate cell-to-cell metabolic communication in order to promote pro-tumoral activities.

Increased GLS1 expression and glutamine metabolism are critical for metabolic reprogramming and sustaining pro-tumoral activities in a stiff environment.

Gln is a precursor of several non-essential amino acids (NEAA) and an anaplerotic carbon source for the TCA cycle in cancer cells (Hensley et al., 2013). However, since Gln can be used in a cell type-specific manner, and CAFs rely upon a different metabolism than CCs (Ghesquière et al., 2014), we explored whether CC and CAF differentially used Gln (**Fig.2** and **Fig.S3**). Treatment of cells with 2 mM U-$^{13}C_5$- Gln led to a 3–5-fold increase of Gln uptake and Gln conversion to Glu upon stiff matrix exposure (**Fig.2A-B**). While in CCs, stiffness did not increase the contribution of carbon from Gln to the TCA cycle (**Fig.2A**), in CAFs, Gln was a major source of carbon for the TCA cycle; ^{13}C was predominantly incorporated into α-ketoglutarate and succinate, and, to a lesser extent, malate and fumarate, as well as the NEAA Asp (**Fig.2B**), a molecule biosynthesized from TCA cycle intermediates (Birsoy et al., 2015; Sullivan et al., 2015). Importantly, while in CAFs, Gln-derived carbon accumulated in Asp with increased stiffness (**Fig.2B**), in CCs, Gln-derived

carbon fed Glu synthesis but failed to feed the TCA cycle and Asp biosynthesis (**Fig..2A**). Correspondingly, inhibition of GLS1 by either a siRNA specific to GLS1 (**Fig.2C** and **Fig.2F**) or a pharmacological inhibitor of GLS1 (CB839) decreased Gln metabolism in both CCs (**Fig.2D and FigS3A-B**) and CAFs (**Fig.2G**) as well as decreased secretion of Glu by CCs (**Fig.2E**) and decreased secretion of Asp by CAFs (**Fig.2H**). Conversely, overexpression of GLS1 (pGLS1) was sufficient to increase the rate of Glu (**Fig.S3G-H**) and Asp (**Fig.S3L-M**) secretion by CCs and CAFs respectively, even if cells were cultivated on soft matrix.

We next investigated whether GLS1 inhibition controlled tumor cell activities. Consistent with prior observations (Gross et al., 2014), GLS1 inhibition, achieved via siRNA or CB839, reduced CC proliferation (**Fig.S3C-F**) and CAF contractility (**Fig.S3J-K)**. Importantly, in cells with decreased GLS1 activity, cellular proliferation and contractility were restored by Asp and Glu supplementation, respectively. Finally, we investigated whether such metabolic crosstalk-dependent cell proliferation (**Fig.2I**) and contractility (**Fig.2J**) were also affected by GLS1 inhibition. Consistent with our metabolic results (**Fig.2E,H**), CAF-CM from CAF treated with either siRNA GLS1 or CB839 failed to activate CC proliferation (**Fig.2I**). Importantly, addition of exogenous Asp rescued CC proliferation. Moreover, CAF-CM from CAF overexpressing GLS1 and plated on soft matrix activated CC proliferation (**Fig.S3N**). Similar results were obtained in CAFs (**Fig.2J and Fig.S3I**). Thus, the stiffness-dependent increase of GLS1 is important for both cell-autonomous pro-tumoral activities and tumor cell crosstalk through the control of Glu and Asp synthesis.

To interrogate whether metabolic crosstalk within a microenvironment is crucial for tumor progression, we performed three-dimensional co-culture invasion assays (spheroid) where GLS1 inhibition was achieved either in CAFs, CCs, or both (**Fig.2K**). Inhibition of GLS1 in either CAF or CC failed to block invasion, while GLS1 inhibition in both CAFs and CCs hampered cell invasion. Importantly, addition of Asp/Glu rescued tumor cells invasion. Collectively, these results argue for a crucial role of Gln-dependent Asp and Glu exchange

between CAFs and CCs in order to shape a pro-invasive tumor niche and sustain pro-tumoral activities.

Aspartate feeds the nucleotide biosynthesis pathway in CCs, while glutamate feeds the glutathione pathway in CAFs.

We next investigated how CCs metabolize CAF-derived Asp (**Fig.3A**). Treatment of cells with 5 mM U-$^{13}C_4$-Asp led to a 2-3-fold increase in the intracellular Asp pool, even in the presence of 2 mM Gln and 4.5 g/L glucose. Carbon from Asp did not contribute to upstream glycolytic intermediates (**data not shown**) and it contributed minimally to the TCA cycle (**Fig.3A**). Another important role of Asp in proliferating cells is to maintain nucleotide synthesis (Sullivan et al., 2015). Thus, we hypothesize that CAF-derived Asp is essential to sustain nucleotide biosynthesis in cancer cells exposed to stiff conditions. Indeed, in stiff matrix, Asp served as an important carbon source for pyrimidine synthesis (**Fig.3A**).

We then performed U-^{13}C-Glu tracing studies to assess how Glu was being used in CAF metabolism (**Fig.3B**). Exposure of cells with 5 mM U-^{13}C-Glu led to a 2-3-fold increase in the intracellular Glu pool, even in presence of 2 mM Gln and 4.5 g/L glucose. Carbon from Glu did not contribute to upstream Gln synthesis (**Fig.3B**). Similar to Gln, carbon from Glu was incorporated to the TCA cycle. While stiffness modestly increased the amount of carbon from Glu contributing to the TCA cycle, the ^{13}C label was markedly incorporated into the glutathione pathway on stiff matrix (**Fig.3B**). These results suggested that CC-derived Glu is used in CAFs to maintain redox homeostasis.

We next investigated whether CC-derived Glu can balance the redox state of CAFs. In stiff conditions, total glutathione (GSH+GSSG) and reduced glutathione (GSH) were decreased in CAFs (**Fig.3C**) and corresponded with an accumulation of reactive oxygen species (ROS) and superoxide (**Fig.3D**). Treatment with either CC-CM or Glu rescued these features. Correspondingly, an increase of F-actin bundles as well as an increase of P-MLC2 were

observed in CAFs treated with CC-CM or Glu (**Fig.3E**), suggesting the induction of cell contractility (as measured in similar conditions, **Fig.1M**).

SLC1A3 enables aspartate/glutamate exchange within the tumor niche to promote tumor progression.

To determine whether Asp/Glu exchange between CAF and CCs is a key step for tumor progression, we sought to identify a cell surface transporter responsible for mediating this exchange (**Fig.3F-G**). Specifically, we hypothesized that such a transporter should be expressed in both CAFs and CCs, over-expressed in CCs cultivated on stiff matrix (**Fig.3F**), and over-expressed in CAFs compared with normal fibroblasts (**Fig.3G**). RT-qPCR screening of the Asp/Glu transporter family members (SLC1A1-7) identified SLC1A3. To determine whether SLC1A3 is responsible of metabolic crosstalk between CAFs and CCs, we assessed the Asp and Glu consumption rate (**Fig.S4C,G**), as well as the intracellular level of Asp and Glu of SLC1A3 knockout tumor cells treated with conditioned media. Upon SLC1A3 inhibition (**Fig.S4A,E**), both Asp consumption rate (**Fig.S4C**) and Glu consumption rate (**Fig.S4G**) were decreased in CCs and CAFs, respectively. Accordingly, a decrease of the intracellular levels of Asp and Glu was also observed (**Fig.S4D,H**).

We next questioned whether Asp/Glu exchange through SLC1A3 is critical to sustain pro-tumoral activities of CCs (**Fig.3H** and **Fig.S4I-J**) and CAFs (**Fig.3I** and **Fig.S4L-M**). SLC1A3 inhibition alone, achieved via siRNA or TFB-TBOA, a pharmacologic inhibitor of SLC1A1-3 family, modestly affected CC proliferation. Importantly, simultaneous inhibition of GLS1 and SLC1A3 prevented Asp/Glu rescue of CC proliferation (**Fig.3H** and **Fig.S4I-J**). Similar to CC, inhibition of SLC1A3 in CAF modestly altered the generation of contractile forces and slightly decreased ECM remodeling. Importantly, pharmacologic or genetic inhibition of GLS1 and SLC1A3 together in CAF blunted Glu rescue of CAF pro-tumoral responses (**Fig.3I** and **Fig.S3L-M**).

We next interrogated whether inhibition of metabolic crosstalk in the tumor niche is sufficient to blunt tumor progression (**Fig.3J and FigS4N-O**). Consistent with our prior findings, in 3D co-culture assay, siRNA knockdown of SLC1A3 alone in CAFs or CCs was not sufficient to impair cellular invasion (**Fig.3J**). In contrast, siRNA knockdown of SLC1A3 alone in both CAFs and CCs or siRNA knockdown of SLC1A3 and GLS1 together in these cells blunted cancer cell invasion (**Fig.3J)**. Similar results were obtained with pharmacologic inhibitors of SLC1A3 and GLS1 (**Fig.S4N-O**). Next, we assessed whether overexpression of SLC1A3 and/or GLS1 are sufficient to activate cancer cell invasion even in a soft tumor niche (**Fig.3K**). In a low collagen microenvironment (1 mg/mL), cancer cells were not able to invade even in presence of CAFs. Overexpression of both GLS1 and SLC1A3 in CCs modestly activated cell invasion. Addition of ribose to increase collagen stiffness also slightly increased cell invasion, a feature that was accentuated by GLS1 and SLC1A3 overexpression in CCs. Taken together, these results demonstrate the crucial role of tumor niche amino acid crosstalk in tumor progression through the mechanical activation of SLC1A3.

Modulation of YAP/TAZ-dependent mechanotransduction pathway controls metabolic reprogramming of tumor cells.

Given our prior findings demonstrating mechanotransduction coordinates glycolysis and glutaminolysis in response to mechanical stress in the lung vasculature (Bertero et al., 2016), we next investigated whether manipulation of the mechanotransduction cascade (**Fig.S5A**) affects the metabolic reprogramming and consequent behavior of tumor niche cells. In tumor cells, pharmacologic inhibition of FAK (PF573228), ROCK (Y27632), or YAP/TAZ (verteporfin) decreased glycolysis (**Fig.S5B,F**) and blunted the effects of tumor niche stiffening on amino acid secretion/consumption (**Fig.S5C,G**). Correspondingly, GLS1, LDHA and SLC1A3 protein expression were downregulated upon pharmacologic inhibition (**Fig.S5D,H**) and siRNA knockdown of YAP/TAZ (**Fig.4A-B**). Importantly, overexpression of YAP was sufficient to induce the protein expression of GLS1, LDHA and SLC1A3, even if

cells were cultivated on soft matrix (**Fig.4A-B**). Since ECM stiffening also activates cell proliferation (Pickup et al., 2014) a known regulator of cell metabolism (DeBerardinis et al., 2008), and in order to uncouple mechano-dependent proliferation and the mechano-dependent metabolic reprogramming, we developed an *in vitro* system in which mechanotransduction could be activated without affecting cell proliferation (**Fig.4C-H**). Cells were cultivated on soft hydrogel with magnetic beads coated with collagen I. Mechanotransduction was then activated by pulling on integrins by adding a magnet. Using this system, we demonstrated that activation of mechanotransduction re-localized YAP/TAZ to the nucleus as well as activated the transcription of GLS1, SLC1A3, along with known YAP-dependent genes CTGF and CYR61 (but not the negative control, GAPDH; **Fig.4C-D, F-G**). Correspondingly, GLS1 and SLC1A3 expression was downregulated in cells upon siRNA knockdown of YAP/TAZ (**Fig.4E,H**). Finally, several putative binding sites for YAP/TAZ complexes (TEAD sites) were revealed by sequence analysis of the promoter regions of GLS1 and SLC1A3 (**Fig4I**). ChIP–quantitative PCR demonstrated the direct binding of YAP on at least one site for each gene (**Fig.4J-K**). Taken together, YAP and TAZ are integral to the mechano-triggered metabolic reprogramming events initiated by ECM stiffness.

We next interrogated whether metabolic crosstalk between CAFs and CCs is also affected by the YAP/TAZ dependent-mechanotransduction pathway. In the first instance, we determined whether inhibition of YAP/TAZ during the medium conditioning process altered its composition. Indeed, inhibition of YAP/TAZ decreased Gln uptake in both cells (**Fig.S5E,I**) and decreased Asp secretion and Glu uptake in CAFs (**Fig.S5I)**, while inhibiting Glu secretion and Asp uptake in CCs (**Fig.S5E**). Consistent with these results, CAF-CM from CAF transfected with siYAP/TAZ failed to activate CC proliferation (**Fig.S5J**). Conversely, CC-CM from CCs transfected with siYAP/TAZ failed to activate CAF contraction (**Fig.S5K**). Importantly, addition of exogenous Asp or Glu rescued CC proliferation and CAF contractility, respectively.

Altogether, we conclude that the YAP-TAZ-dependent mechanotransduction cascade is integral to the stiffness-induced metabolic reprogramming of the tumor niche.

The mechanotransduction cascade controls metabolic reprogramming of tumor niche cells *in vivo*.

To establish definitively whether tumor niche remodeling and stiffening modulate tumor cells metabolism and behavior *in vivo*, we tested whether alteration of the mechanotransduction cascade directly controls Gln metabolism and tumor progression in an orthotopic syngenic mouse model of a highly metastatic breast cancer (**Fig.5** and **Fig.S6**). First, using the well-established Balb/c mammary tumor cell lines 67NR, 410.4 and 4T1, we determined whether ECM-dependent metabolic changes were conserved (**Fig.S6A-F**). As reflected by LC-MS analysis, ECM stiffening increased glycolysis, Gln metabolism and Asp production as well as increased GLS1, LDHA, and SLC1A3 expression (**Fig.S6A-F**).

Second, using a known pharmacologic inhibitor (β-aminopropionitrile, BAPN) of lysyl-oxidase (Lox), the enzyme responsible for collagen cross-linking and consequent matrix stiffening (Levental et al., 2009), or verteporfin, a known pharmacologic inhibitor of YAP (Park and Guan, 2013), we determined whether inhibition of mechanotransduction could prevent metabolic changes and tumor progression in mice (**Fig.5A**). Either BAPN or verteporfin treatments decreased Lox activity (**Fig.S6G**) and consequent ECM stiffening (**Fig.5B**). Consistent with our *in vitro* results, inhibition of mechanotransduction by BAPN or verteporfin led to a decrease of GLS1 and SLC1A3 expression (**FigS5H** and **Fig.5F-G**), and downstream GLS activity, as reflected by enzymatic activity measurement (**Fig.5C**) and intratumoral levels of Asp (**Fig.5D**) and Glu (**Fig.5E**). Such metabolic effects further decreased tumor cell proliferation (**Fig.5F-G**) and improved end-stage manifestations of breast cancer, including reductions of tumor volume (**Fig.5H**), lung metastasis (**Fig.5I-J**), and survival (**Fig.5K**). As a result, these data provide causative evidence *in vivo* that tumor niche

stiffening relies on mechanotransduction pathways to induce tumor cell Gln metabolism and glycolysis, proliferation, invasion, and overall survival outcome.

Aspartate/glutamate exchanges within the tumor niche are crucial to sustain tumor progression *in vivo.*

We next determined whether amino acid exchange was occurring in the tumor microenvironment *in vivo*. We developed a co-injection system in which CAF could be manipulated genetically and then implanted alongside cancer cells into the mammary fat pads of syngeneic mice. Although our previous study demonstrated that co-injection of CAF with non-invasive 67NR cells promotes tumor growth and local invasion (Albrengues et al., 2015), the contribution of metabolic cross-talk to this effect has not been explored. Therefore, we performed co-injection studies with 67NR cells along with CAF with conditional knockdown of SLC1A3 and GLS1, separately or together. Fifteen day after cells injections mice were treated with doxycycline in order to induce depletion of GLS1 and/or SLC1A3 in stromal fibroblast (**Fig.S7A-B**). Consistent with the *in vitro* 3D assay data (**Fig.4**), while GLS1 or SLC1A3 knockdown slightly decreased tumor cell invasion (**Fig.6B-C**), tumor cell proliferation (**Fig.6C**) and ECM remodeling (**Fig.6C)** combine treatment led to a greater inhibition.

We next investigated whether the reciprocal mechanism was also effective *in vivo*. Consistent with our findings (**Fig.6**) and a previous report (Yang et al., 2004), 4T1 cells promoted tumor invasion by converting resident fibroblasts into CAF. However, the contribution of metabolic crosstalk to this effect has not been explored. Thus, we injected 4T1 cells with conditional knockdown of SLC1A3, GLS1, or SLC1A3 and GLS1 together into the mammary fat pads of syngeneic mice (**Fig.6D**). Either GLS1 or SLC1A3 knockdown alone decreased tumor cell proliferation and inhibited 4T1 tumor progression, (**Fig.6D-G**). Notably, combined treatment led to a greater inhibition of tumor growth and invasion and further improved survival (**Fig.6H**). To determine whether inhibition of metastasis was

dependent on organ colonization or metastasic growth, we performed tail vein injections of 4T1 cells undergoing conditionally knock-down for SLC1A3, GLS1 or both SLC1A3 and GLS1. Induction of knockdown was performed before tail vein injection (**Fig.S7E-G**) or after lung colonization (**Fig.S7H-J**) in order to determine the effect of gene knockdown on lung colonization or metastatic growth, respectively. Inhibition of SLC1A3 affected lung colonization while inhibition of GLS1 affected cell growth. Importantly, inhibition of both GLS1 and SLC1A3 drastically decreased cell growth and lung colonization. Altogether, these data provide evidence that GLS1 and SLC1A3 inhibition affects multiple sequential steps of tumor progression *in vivo*.

Finally, we investigated whether pharmacological inhibition of both glutaminolysis and Asp/Glu exchange are relevant therapies for cancer. We performed combination treatments in the highly metastatic orthotopic syngeneic 4T1 breast cancer mouse model (**Fig.46I)**. Whereas either CB839 or TFB-TBOA treatment alone inhibited 4T1 tumor progression (**Fig.6J-L** and **Fig.S7K)** and decreased tumor cell proliferation (**Fig.6M**), combined treatment led to greater inhibition of tumor growth and invasion and further improved survival outcomes (**Fig.6J-L**). In sum, these data provide evidence for a two-way intratumoral metabolic cross-talk, which could be pharmacologically targeted to blunt tumor progression.

GLS1 and SLC1A3 are highly expressed in HNSCC tumors and are *bona fide* targets for therapy in patients with HNSCC.

Finally, on the basis of these findings in mice, we wanted to determine whether humans suffering from SCC may also display signs of increased ECM stiffness and consequent alterations in glutaminolysis and Asp/Glu transport and thus may also be sensitive to these combined therapies. We first studied whether GLS1 and SLC1A3 are also induced in human head and neck squamous cell carcinoma (HNSCC) tumors. Analysis of The Cancer Genome Atlas (TCGA) head and neck carcinoma data set (**Fig.7A-D**) revealed that GLS1 mRNA was significantly elevated in primary HNSCC tumors (n=497) as compared with adjacent normal

tissues (n=44; **data not shown**). GLS1 (**Fig.7A**) and SLC1A3 mRNA (**Fig.7C**) were upregulated in histological grades 1–4 of human HNSCC. Kaplan-Meier analysis of the TCGA data set revealed that high levels of GLS1 mRNA (**Fig.7B**) – but not SLC1A3 (**Fig.7D**) – were associated with poor overall survival of patients with HNSCC. Second, we performed immunohistochemistry assays to confirm GLS1 and SLC1A3 induction directly in human HNSCC tumors (**Fig.7E-H**). Based on tumor invasiveness, a cohort of 48 patients with pathological diagnosis of HNSCC was stratified into 3 cohorts (low, N=15; middle, N=11; high N=22). Correlating with increased collagen remodeling in highly invasive cases, a concurrent upregulation of GLS1 and SLC1A3 was observed (**Fig.7E-H)**). Together, these data indicate that GLS1 and SLC1A3 are highly expressed in HNSCC tumors and GLS1 is associated with worse clinical outcomes in patients with HNSCC cancer, suggesting a possible therapeutic benefit for targeting these molecules.

To test this idea, a patient-derived spheroid (PDS) model of HNSCC was developed (**Fig.7I-J)**. Seven independent HNSCC tumors were embedded in a rich collagen microenvironment, and 3D invasion assessed. Correlating with our observations in cell lines, either CB839 or TFB-TBOA treatment alone in PDS blunted tumor cell invasion. Combined treatment led to a greater inhibition (**Fig.7I-J)**. To test this hypothesis even further, a patient-derived xenograft (PDX) model of HNSCC expansion was explored *in vivo* (**Fig.7K-M**). Three independent HNSCC tumors were subcutaneously engrafted in the flanks of nude mice. One week later, once the tumors were established, mice were treated with vehicle control, CB839, BPTES, TFB-TBOA or a combination of these drugs. Consistent with our *in vitro* and *in vivo* results, either CB839 or TFB-TBOA treatment alone in the PDX model of HNSCC blunted tumor growth **(Fig.7K**) and decreased tumor cell proliferation (**Fig.7L-M**). Importantly, combined treatment more robustly inhibited tumor growth. Taken together, these results directly implicate GLS1 and SLC1A3 within the tumor niche -- two processes dependent on ECM stiffening -- as critical metabolic mediators necessary for sustaining tumor cell activation and cancer progression

Discussion

While prior context-specific studies have demonstrated metabolic crosstalk within the tumors (Commisso et al., 2013; Davidson et al., 2017; Perera et al., 2015; Sousa et al., 2016; Yang et al., 2016), the role of mechanotransduction in this process has never been explored previously. To decode this regulatory pathway, we adopted an approach where differential metabolic transformations in reactive stroma (stiff ECM) versus healthy stroma (soft ECM; **Fig.1**) were identified. Among these metabolites, we found Asp production by CAF crucial to sustain CCs proliferation. Consistent with these results, recent reports have shown that aspartate acquisition is a metabolic limitation encountered by tumors in their native *in vivo* environment and that overcoming this limitation is advantageous for tumour growth(Garcia-Bermudez et al., 2018; Sullivan et al., 2018). Together, our results clarify the importance of Asp in tumor progression and demonstrate a fine-tuneable mechanism by which CCs are able to adjust their Asp needs depending on tumor niche stiffness.

In tumor niche contexts, YAP/TAZ have been reported to control cell proliferation and contractility in response to the mechanical cues from the environment (Calvo et al., 2013; Dupont et al., 2011). Here, our findings define the mechanotransduction cascade mediated via YAP/TAZ as a lynchpin between biophysical cues and the metabolic adaptations required for growth in the stiff tumor microenvironment. This reciprocity among YAP/TAZ with upstream (Enzo et al., 2015; Mo et al., 2015; Sorrentino et al., 2014; Wang et al., 2015) and downstream metabolic cues suggests an adjustable, feedback-driven property inherent to this pathway (Bertero et al., 2015a, 2015b; Calvo et al., 2013) and may be partly responsible for individualized “tuning” of the metabolic program within the tumor.

Finally, targeting tumor stroma for therapeutic purpose is a burgeoning idea that is gaining traction recently (Kalluri, 2016; Quail and Joyce, 2013). However, therapeutic use of specific stroma inhibitors alone may suffer from modest efficacy. Identification of glutaminolysis and Asp/Glu communication through the same co-transporter (i.e., SLC1A3)

as a shared metabolic program by CAF and CC presents a viable opportunity to offer novel therapeutics in these diseases via targeting, with the same compound, both stromal and tumor cells.

Together, these results carry broad implications for our fundamental understanding of how cells adjust their energetic demands based on extracellular mechanical cues. These findings endorse the rapid application of novel pharmacologic inhibitors to target the metabolic effects of matrix stiffness and thus prevent cancer progression. Moreover, such translational studies in highly desmoplastic carcinoma may have broad applications to other human metabolic conditions in which such mechanosensitive interactions may serve as crucial origins of disease.

Limitations of study

In sum, our findings from combined pharmacologic, molecular, and genetic studies in diverse preclinical models of SCC define the mechano-dependent metabolic rewiring of tumor niche as a central pathogenic mechanism by which matrix stiffness can stimulate pro-tumoral activity. Importantly, while this report focuses mainly on glutaminolysis/anaplerotic pathways, our experiments focused specifically on few metabolites and biochemical pathways. Thus, the true breadth of influence by tumor niche stiffness in metabolic reprogramming may be even more extensive. Moreover, while we identified CC-CAF amino acid crosstalk as a key mechanism to sustain tumor progression in response to ECM stiffness, it will be crucial to determine whether similar metabolic crosstalk occurs among other cells within the tumor niche. Resolution at the single-cell scale and development of single-cell metabolomics will be critically important to deciphering the metabolic architecture of tumors.

Acknowledgments

We thank J. Muller for bioinformatics assistance. The authors acknowledge the IRCAN's Molecular and Cellular Core Imaging (PICMI), the histology, the genomic and animal housing Facilities (supported by le Cancéropole PACA, la Région PACA, le Conseil Départementale 06, l'INSERM, ARC, IBiSA, and the Conseil Départemental 06 de la Région PACA). This work was supported by; the Ligue Nationale contre le Cancer and the SILAB foundation (to T.B.); the French National Research Agency (ANR-11-LABX-0028-01) and Association pour la Recherche sur le Cancer (ARC) grant PJA20131200325 (to C.G. and T.B) as well as Fondation pour la Recherche Medicale (FRM) grant DEQ20180339183 (to C.G.); NIH grants R01 HL124021, HL 122596, HL 138437, and UH2 TR002073 as well as American Heart Association grant 18EIA33900027 (to S.Y.C); NIH grant HL128802 (to W.M.O). MetaToul is part of the national infrastructure MetaboHUB-ANR-11-INBS-0010

Author contributions

TB, WMO, and CG conceived and designed the experiments. TB, WMO, SYC, EF, IB, CCF, GM, DVB and CG provided the experimental infrastructure and performed the experiments. FB performed and analyzed ^{13}C tracing experiments. AB, PH and CG obtained human samples. SP performed atomic force microscopy analysis. EB and SE provide protocols, reagents and assistances for TFM and magnetic bead force assays. TB and CCF performed mouse experiments. TB, WMO, SYC, and CG wrote the manuscript. All authors participated in interpreting the results and revising the manuscript.

Declaration of interests

The authors declare no competing interests

References

Albrengues, J., Meneguzzi, G., and Gaggioli, C. (2013). Analysis of collective invasion of carcinoma cells in a 3D organotypic model. Methods Mol. Biol. Clifton NJ *961*, 243–252.

Albrengues, J., Bourget, I., Pons, C., Butet, V., Hofman, P., Tartare-Deckert, S., Feral, C.C., Meneguzzi, G., and Gaggioli, C. (2014). LIF mediates proinvasive activation of stromal fibroblasts in cancer. Cell Rep. *7*, 1664–1678.

Albrengues, J., Bertero, T., Grasset, E., Bonan, S., Maiel, M., Bourget, I., Philippe, C., Herraiz Serrano, C., Benamar, S., Croce, O., et al. (2015). Epigenetic switch drives the conversion of fibroblasts into proinvasive cancer-associated fibroblasts. Nat. Commun. *6*, 10204.

Bays, J.L., Campbell, H.K., Heidema, C., Sebbagh, M., and DeMali, K.A. (2017). Linking E-cadherin mechanotransduction to cell metabolism through force-mediated activation of AMPK. Nat. Cell Biol. *19*, 724–731.

Ben-Sahra, I., and Manning, B.D. (2017). mTORC1 signaling and the metabolic control of cell growth. Curr. Opin. Cell Biol. *45*, 72–82.

Bertero, T., Cottrill, K.A., Annis, S., Bhat, B., Gochuico, B.R., Osorio, J.C., Rosas, I., Haley, K.J., Corey, K.E., Chung, R.T., et al. (2015a). A YAP/TAZ-miR-130/301 molecular circuit exerts systems-level control of fibrosis in a network of human diseases and physiologic conditions. Sci. Rep. *5*, 18277.

Bertero, T., Cottrill, K.A., Lu, Y., Haeger, C.M., Dieffenbach, P., Annis, S., Hale, A., Bhat, B., Kaimal, V., Zhang, Y.-Y., et al. (2015b). Matrix Remodeling Promotes Pulmonary Hypertension through Feedback Mechanoactivation of the YAP/TAZ-miR-130/301 Circuit. Cell Rep. *13*, 1016–1032.

Bertero, T., Oldham, W.M., Cottrill, K.A., Pisano, S., Vanderpool, R.R., Yu, Q., Zhao, J., Tai, Y., Tang, Y., Zhang, Y.-Y., et al. (2016). Vascular stiffness mechanoactivates YAP/TAZ-dependent glutaminolysis to drive pulmonary hypertension. J. Clin. Invest. *126*, 3313–3335.

Birsoy, K., Wang, T., Chen, W.W., Freinkman, E., Abu-Remaileh, M., and Sabatini, D.M. (2015). An Essential Role of the Mitochondrial Electron Transport Chain in Cell Proliferation Is to Enable Aspartate Synthesis. Cell *162*, 540–551.

Calvo, F., Ege, N., Grande-Garcia, A., Hooper, S., Jenkins, R.P., Chaudhry, S.I., Harrington, K., Williamson, P., Moeendarbary, E., Charras, G., et al. (2013). Mechanotransduction and YAP-dependent matrix remodelling is required for the generation and maintenance of cancer-associated fibroblasts. Nat. Cell Biol. *15*, 637–646.

Commisso, C., Davidson, S.M., Soydaner-Azeloglu, R.G., Parker, S.J., Kamphorst, J.J., Hackett, S., Grabocka, E., Nofal, M., Drebin, J.A., Thompson, C.B., et al. (2013). Macropinocytosis of protein is an amino acid supply route in Ras-transformed cells. Nature *497*, 633–637.

Davidson, S.M., Jonas, O., Keibler, M.A., Hou, H.W., Luengo, A., Mayers, J.R., Wyckoff, J., Del Rosario, A.M., Whitman, M., Chin, C.R., et al. (2017). Direct evidence for cancer-cell-autonomous extracellular protein catabolism in pancreatic tumors. Nat. Med. *23*, 235–241.

DeBerardinis, R.J., Lum, J.J., Hatzivassiliou, G., and Thompson, C.B. (2008). The Biology of Cancer: Metabolic Reprogramming Fuels Cell Growth and Proliferation. Cell Metab. *7*, 11–20.

Dupont, S., Morsut, L., Aragona, M., Enzo, E., Giulitti, S., Cordenonsi, M., Zanconato, F., Le Digabel, J., Forcato, M., Bicciato, S., et al. (2011). Role of YAP/TAZ in mechanotransduction. Nature *474*, 179–183.

Enzo, E., Santinon, G., Pocaterra, A., Aragona, M., Bresolin, S., Forcato, M., Grifoni, D., Pession, A., Zanconato, F., Guzzo, G., et al. (2015). Aerobic glycolysis tunes YAP/TAZ transcriptional activity. EMBO J. *34*, 1349–1370.

Gaggioli, C., Hooper, S., Hidalgo-Carcedo, C., Grosse, R., Marshall, J.F., Harrington, K., and Sahai, E. (2007). Fibroblast-led collective invasion of carcinoma cells with differing roles for RhoGTPases in leading and following cells. Nat. Cell Biol. *9*, 1392–1400.

Garcia-Bermudez, J., Baudrier, L., La, K., Zhu, X.G., Fidelin, J., Sviderskiy, V.O., Papagiannakopoulos, T., Molina, H., Snuderl, M., Lewis, C.A., et al. (2018). Aspartate is a limiting metabolite for cancer cell proliferation under hypoxia and in tumours. Nat. Cell Biol. *20*, 775–781.

Ghesquière, B., Wong, B.W., Kuchnio, A., and Carmeliet, P. (2014). Metabolism of stromal and immune cells in health and disease. Nature *511*, 167–176.

Gross, M.I., Demo, S.D., Dennison, J.B., Chen, L., Chernov-Rogan, T., Goyal, B., Janes, J.R., Laidig, G.J., Lewis, E.R., Li, J., et al. (2014). Antitumor activity of the glutaminase inhibitor CB-839 in triple-negative breast cancer. Mol. Cancer Ther. *13*, 890–901.

Guilluy, C., Swaminathan, V., Garcia-Mata, R., O'Brien, E.T., Superfine, R., and Burridge, K. (2011). The Rho GEFs LARG and GEF-H1 regulate the mechanical response to force on integrins. Nat. Cell Biol. *13*, 722–727.

Hanahan, D., and Weinberg, R.A. (2011). Hallmarks of cancer: the next generation. Cell *144*, 646–674.

Hensley, C.T., Wasti, A.T., and DeBerardinis, R.J. (2013). Glutamine and cancer: cell biology, physiology, and clinical opportunities. J. Clin. Invest. *123*, 3678–3684.

Hensley, C.T., Faubert, B., Yuan, Q., Lev-Cohain, N., Jin, E., Kim, J., Jiang, L., Ko, B., Skelton, R., Loudat, L., et al. (2016). Metabolic Heterogeneity in Human Lung Tumors. Cell *164*, 681–694.

Heuillet, M., Bellvert, F., Cahoreau, E., Letisse, F., Millard, P., and Portais, J.-C. (2018). Methodology for the Validation of Isotopic Analyses by Mass Spectrometry in Stable-Isotope Labeling Experiments. Anal. Chem. *90*, 1852–1860.

Kai, F., Laklai, H., and Weaver, V.M. (2016). Force Matters: Biomechanical Regulation of Cell Invasion and Migration in Disease. Trends Cell Biol. *26*, 486–497.

Kalluri, R. (2016). The biology and function of fibroblasts in cancer. Nat. Rev. Cancer *16*, 582–598.

Levental, K.R., Yu, H., Kass, L., Lakins, J.N., Egeblad, M., Erler, J.T., Fong, S.F.T., Csiszar, K., Giaccia, A., Weninger, W., et al. (2009). Matrix crosslinking forces tumor progression by enhancing integrin signaling. Cell *139*, 891–906.

Liu, F., Haeger, C.M., Dieffenbach, P.B., Sicard, D., Chrobak, I., Coronata, A.M.F., Suárez Velandia, M.M., Vitali, S., Colas, R.A., Norris, P.C., et al. (2016). Distal vessel stiffening is an early and pivotal mechanobiological regulator of vascular remodeling and pulmonary hypertension. JCI Insight *1*.

Millard, P., Letisse, F., Sokol, S., and Portais, J.-C. (2012). IsoCor: correcting MS data in isotope labeling experiments. Bioinforma. Oxf. Engl. *28*, 1294–1296.

Mo, J.-S., Meng, Z., Kim, Y.C., Park, H.W., Hansen, C.G., Kim, S., Lim, D.-S., and Guan, K.-L. (2015). Cellular energy stress induces AMPK-mediated regulation of YAP and the Hippo pathway. Nat. Cell Biol. *17*, 500–510.

Oldham, W.M., Clish, C.B., Yang, Y., and Loscalzo, J. (2015). Hypoxia-Mediated Increases in l-2-hydroxyglutarate Coordinate the Metabolic Response to Reductive Stress. Cell Metab. *22*, 291–303.

Park, H.W., and Guan, K.-L. (2013). Regulation of the Hippo pathway and implications for anticancer drug development. Trends Pharmacol. Sci. *34*, 581–589.

Perera, R.M., Stoykova, S., Nicolay, B.N., Ross, K.N., Fitamant, J., Boukhali, M., Lengrand, J., Deshpande, V., Selig, M.K., Ferrone, C.R., et al. (2015). Transcriptional control of autophagy-lysosome function drives pancreatic cancer metabolism. Nature *524*, 361–365.

Pickup, M.W., Mouw, J.K., and Weaver, V.M. (2014). The extracellular matrix modulates the hallmarks of cancer. EMBO Rep. *15*, 1243–1253.

Quail, D.F., and Joyce, J.A. (2013). Microenvironmental regulation of tumor progression and metastasis. Nat. Med. *19*, 1423–1437.

Santinon, G., Brian, I., Pocaterra, A., Romani, P., Franzolin, E., Rampazzo, C., Bicciato, S., and Dupont, S. (2018). dNTP metabolism links mechanical cues and YAP/TAZ to cell growth and oncogene-induced senescence. EMBO J.

Sorrentino, G., Ruggeri, N., Specchia, V., Cordenonsi, M., Mano, M., Dupont, S., Manfrin, A., Ingallina, E., Sommaggio, R., Piazza, S., et al. (2014). Metabolic control of YAP and TAZ by the mevalonate pathway. Nat. Cell Biol. *16*, 357–366.

Sousa, C.M., Biancur, D.E., Wang, X., Halbrook, C.J., Sherman, M.H., Zhang, L., Kremer, D., Hwang, R.F., Witkiewicz, A.K., Ying, H., et al. (2016). Pancreatic stellate cells support tumour metabolism through autophagic alanine secretion. Nature *536*, 479–483.

Sullivan, L.B., Gui, D.Y., Hosios, A.M., Bush, L.N., Freinkman, E., and Vander Heiden, M.G. (2015). Supporting Aspartate Biosynthesis Is an Essential Function of Respiration in Proliferating Cells. Cell *162*, 552–563.

Sullivan, L.B., Gui, D.Y., and Vander Heiden, M.G. (2016). Altered metabolite levels in cancer: implications for tumour biology and cancer therapy. Nat. Rev. Cancer *16*, 680–693.

Sullivan, L.B., Luengo, A., Danai, L.V., Bush, L.N., Diehl, F.F., Hosios, A.M., Lau, A.N., Elmiligy, S., Malstrom, S., Lewis, C.A., et al. (2018). Aspartate is an endogenous metabolic limitation for tumour growth. Nat. Cell Biol. *20*, 782–788.

Tseng, Q., Duchemin-Pelletier, E., Deshiere, A., Balland, M., Guillou, H., Filhol, O., and Théry, M. (2012). Spatial organization of the extracellular matrix regulates cell-cell junction positioning. Proc. Natl. Acad. Sci. U. S. A. *109*, 1506–1511.

Vander Heiden, M.G., and DeBerardinis, R.J. (2017). Understanding the Intersections between Metabolism and Cancer Biology. Cell *168*, 657–669.

Wang, W., Xiao, Z.-D., Li, X., Aziz, K.E., Gan, B., Johnson, R.L., and Chen, J. (2015). AMPK modulates Hippo pathway activity to regulate energy homeostasis. Nat. Cell Biol. *17*, 490–499.

Watson, I.R., Takahashi, K., Futreal, P.A., and Chin, L. (2013). Emerging patterns of somatic mutations in cancer. Nat. Rev. Genet. *14*, 703–718.

Wiederschain, D., Wee, S., Chen, L., Loo, A., Yang, G., Huang, A., Chen, Y., Caponigro, G., Yao, Y.-M., Lengauer, C., et al. (2009). Single-vector inducible lentiviral RNAi system for oncology target validation. Cell Cycle Georget. Tex *8*, 498–504.

Yang, C.-S., Stampouloglou, E., Kingston, N.M., Zhang, L., Monti, S., and Varelas, X. (2018). Glutamine-utilizing transaminases are a metabolic vulnerability of TAZ/YAP-activated cancer cells. EMBO Rep.

Yang, J., Mani, S.A., Donaher, J.L., Ramaswamy, S., Itzykson, R.A., Come, C., Savagner, P., Gitelman, I., Richardson, A., and Weinberg, R.A. (2004). Twist, a master regulator of morphogenesis, plays an essential role in tumor metastasis. Cell *117*, 927–939.

Yang, L., Achreja, A., Yeung, T.-L., Mangala, L.S., Jiang, D., Han, C., Baddour, J., Marini, J.C., Ni, J., Nakahara, R., et al. (2016). Targeting Stromal Glutamine Synthetase in Tumors Disrupts Tumor Microenvironment-Regulated Cancer Cell Growth. Cell Metab. *24*, 685–700.

Yu, F.-X., Zhao, B., and Guan, K.-L. (2015). Hippo Pathway in Organ Size Control, Tissue Homeostasis, and Cancer. Cell *163*, 811–828.

Figure legends

Figure 1: ECM stiffening reprograms tumor niche cell metabolism and coordinates amino acid exchange to fuel pro-tumoral activities. A) Extracellular flux analyses of SCC12 plated on soft or stiff matrix (mean of 9 wells from 3 independent experiments). **B)** Glucose-derived carbon labeling patterns of metabolites in SCC12 plated on soft (1kPa) or stiff (8kPa) hydrogel and treated with U-$^{13}C_6$-glucose (mean of n=3 independent experiments). **C-D)** Glutamine (Gln) flux (C) and glutamate (glu) and Aspartate (Asp) flux (D) of SCC12 plated on 1kPa or 8kPa hydrogel (n=3). **E)** Extracellular flux analyses of CAF plated on soft or stiff matrix (mean of 9 wells from 3 independent experiments). **F)** Glucose-derived carbon labeling patterns of metabolites in CAFs plated on soft (1kPa) or stiff (8kPa) hydrogel and treated with ^{13}C-glucose (mean of n=3 independent experiments) **G-H)** Gln flux (G) and glu and Asp flux (H) of CAFs plated on 1kPa or 8kPa hydrogel (n=3). **I)** Scheme of the metabolomic experiments for J-K. **J-K)** Metabolites that were significantly elevated in SCC12-conditioned medium (CM), decreased in double-conditioned medium (SCC12-CM added to CAF and then collected), and elevated intracellularly in CAFs treated with SCC12-CM (J, n=3). Metabolites that were significantly elevated in CAF-CM, decreased in double-CM (CAF-CM added to SCC12 cells and then collected), and elevated intracellularly in SCC12 cells treated with CAF-CM (K, n=3). Data normalized to 1kPa **L)** The relative cell numbers of SCC12 cells are shown, cultivated on the indicated substrate in DMEM, 2mM Gln, and the indicated Asp concentration at 72h. Mean of n=9 wells from 3 independent experiments. **M)** Representative pictures and quantification showing change in percent of proliferative (Ki67+) SCC12 plated on stiff (8kPa) substrate 24h after treatment with the indicated conditioned media (CM; n=3). **N)** Quantification by traction force microscopy of contractile forces generated by CAF, cultivated on 8kPa hydrogel in DMEM, 2mM Gln, and following treatment with the indicated Glu concentration. Mean of n=6 wells from 3 independent experiments. **O)** Representative heat map showing contractile forces generate by CAF plated on 8kPa hydrogel following treatment with indicated CM. Mean of n=6 wells from 3 independent experiments. In all panels, data are expressed as the mean ± SD (*P <

0.05, **P < 0.01, ***P < 0.001). Paired samples were compared by 2-tailed Student's t test, while 1-way ANOVA and post-hoc Tukey's tests were used for group comparisons. Scale bars 50µm. **See also Figure S1 and Figure S2.**

Figure 2: Metabolic reprogramming is dependent on glutamine metabolism and GLS1 expression and sustains CAF and SCC pro-tumoral activities. A-B) Gln-derived carbon labeling patterns of metabolites in SCC12s (A) and CAFs (B) plated on soft (1kPa) or stiff (8kPa) hydrogel and treated overnight with U-$^{13}C_5$-Gln (mean of n=3 independent experiments). **C)** Representative image of immunoblot analysis confirming the knockdown of GLS1 by 2 independent siRNA sequences in SCC12s. **D-E)** Intracellular Gln and Glu levels (D) and extracellular Glu level compared to t0 (E) of SCC12 48h after GLS1 inhibition by either siRNAs (siGLS1) or pharmacological inhibitor (CB839; n=3). **F)** Representative images of immunoblot analysis confirming the knockdown of GLS1 by 2 independent siRNA sequences in CAFs. **G-H)** Intracellular Gln and Glu levels (G) and extracellular Asp level compared to t0 (H) in CAFs 48h after GLS1 inhibition by either siRNAs (siGLS1) or a pharmacological inhibitor (CB839; n=3). **I)** Representative pictures and quantification showing change in percent of proliferative (Ki67+) SCC12 cells plated on stiff (8kPa) substrate 24h after treatment with the indicated conditioned media (CM; n=3). **J)** Representative heat map of traction force microscopy experiments showing contractile forces generate by CAF plated on 8kPa hydrogel following treatment with indicated CM. Mean of n=6 wells from 3 independent experiments. **K)** Representative pictures and quantification showing invasion in three-dimensional co-culture assay after the indicated treatment. Mean of at least n=12 spheroid from three independent experiments. In F and I, mean expression in control groups (si-NC) was assigned a fold change of 1 to which relevant samples were compared. Data are expressed as the mean ± SD (*P < 0.05, **P < 0.01, ***P < 0.001) of at least 3 independent experiments. Paired samples were compared by 2-tailed Student's t test, while 1-way ANOVA and post-hoc Tukey's tests were used for group comparisons. Scale bars: In I and J 50µm; in K 400µm **See also Figure S3.**

Figure 3: SLC1A3 enables Aspartate-dependent nucleotide biosynthesis to sustain proliferation in SCCs, while SLC1A3 promotes glutamate-dependent glutathione synthesis to sustain cell contractility in CAFs. A) Asp-derived carbon labeling patterns of metabolites in SCC12 plated on soft (1kPa) or stiff (8kPa) hydrogel and treated overnight with $^{13}C_4$-Asp (mean of n=3 independent experiments). **B)** Glu-derived carbon labeling patterns of metabolites in CAFs plated on soft (1kPa) or stiff (8kPa) hydrogel and treated overnight with $^{13}C_5$-Glu (mean of n=3 independent experiments). **C)** Intracellular level of total glutathione (GSHt) and ratio of GSHt/reduced glutathione (GSH) of CAFs plated on soft (1kPa) or stiff substrate (8kPa) 24h after treatment with the indicated conditioned media (CM). Mean of n=9 wells from three independent experiments. **D)** Representative pictures and quantification showing the intracellular level of ROS and superoxide of CAFs following treatment with the indicated CM**.** Mean of 50 cells from 3 independent experiments. Scale bar: 20µm **E)** Representative pictures and quantification showing the F-actin cytoskeleton rearrangement as well as the P-MLC2 level of CAFs plated on stiff hydrogel (8kPa) following treatment with the indicated CM. Mean of 50 cells from 3 independent experiments. Scale bar 50µm **F)** RT-qPCR analyses of SLC1A family expression in SCC12 plated of soft or stiff substrate (n=4). **G)** RT-qPCR analyses of SLC1A family expression in fibroblasts (n=5) and CAFs (n=5). **H)** Percent of proliferative (PCNA+) SCC12 cells plated on stiff hydrogel 48h after the indicated treatments (n=3). **I)** Quantification by traction force microscopy of contractile forces generated by CAF plated on 8kPa hydrogel following the indicated treatment. Mean of n=6 wells from 3 independent experiments. **J-K)** Representative pictures and quantification showing invasion in three-dimensional co-culture assay after the indicated treatment. Mean of at least n=12 spheroids from three independent experiments. Scale bars 400µm. Data are expressed as the mean ± SD (*P < 0.05, **P < 0.01, ***P < 0.001) of at least 3 independent experiments. Paired samples were compared by 2-tailed Student's t test, while 1-way ANOVA and post-hoc Tukey's tests were used for group comparisons. **See also Figure S4.**

Figure 4: Metabolic reprogramming is coordinated by a YAP/TAZ-dependent mechanotransduction pathway. A-B) Quantification of SLC1A3 and GLS1 protein expression level in SCC12s (A) and CAFs (B) following siRNA-mediated YAP/TAZ knockdown or forced expression of YAP by cells infection with a lentiviral vector containing the YAP coding sequences (pYAP) and compared with cells transfected with a control siRNA (siNC) or with cells infected with a control vector (pGFP), respectively. Representative images of 3 independent experiments were shown. **C-H)** SCC12 cells (C-E) and CAFs (F-H) were plated on soft hydrogel (1kPa) and incubated with magnetic beads coupled to collagen. Representative confocal imaging (C and F) showing YAP/TAZ localization following the indicated treatments (n=3). Red dots: Paramagnetic beads. RT-qPCR revealed increased expression of GLS1 and SLC1A3 after magnet stimulation, but not GAPDH (negative control, D and G). This effect was blunted by YAP/TAZ siRNA knockdown (E and H). **I)** Sequence analysis predicted the presence of TEAD binding sites in the promoter regions (1,500 bp upstream to the start codon) of GLS1 and SLC1A3. **J-K**) ChIP-qPCR confirmed the presence of TEAD/YAP binding sites in the GLS1 and SLC1A3 promoter regions in both SCC12s (J) and CAFs (K). Results are expressed as percentage of total input DNA prior to immunoprecipitation with anti-YAP or anti-IgG control. Means of 3 independent experiments performed in triplicate. CTGF and CYR61, two known YAP targets, were used as positive controls. Data are expressed as the mean ± SD (*P < 0.05, **P < 0.01, ***P < 0.001) of at least 3 independent experiments. Paired samples were compared by 2-tailed Student's t test, while 1-way ANOVA and post-hoc Tukey's tests were used for group comparisons. Scale bars: 50µm. **See also Figure S5.**

Figure 5: Alteration of mechanotransduction affects metabolic reprogramming and tumor progression *in vivo.* A) Following cancer cell implantation, mice were treated with daily BAPN (100 mg/kg; n = 14); with daily i.p. injections of verteporfin (20mg/kg; n = 26) or vehicle, (4T1 cells n=26). 67NR cells were used as control (non-invasive tumor) **B)** Atomic

force microscopy revealed decreased tumor stiffness in BAPN- and verteporfin-treated mice. Data are represented by Tukey boxplots. Median represents at least 70 measures from n=3 mice per group. **C)** Intratumoral GLS activity was measured. Each dot represents a mouse. **D-E)** Tumor cells isolated from the indicated tumors were analyzed for the levels of Asp and glu (data normalized to the 67NR group; each dot represents a single mouse). **F-G)** Representative picrosirius red images (F) and quantification (G) showing the collagen deposition and remodeling as well as representative IHC images (F) and quantification (G) showing GLS1, SLC1A3 and PCNA staining. Each dot represents a mouse. **H-K)** Tumor progression was analyzed as assessed by the tumor volume (H), lung macro metastasis analysis (I-J) and survival outcome (K). Each dot represents a mouse**.** Data are expressed as the mean ± SEM (*P < 0.05, **P < 0.01, ***P < 0.001). Group comparisons were performed by 1-way ANOVA and post-hoc Tukey's tests. Scale bars: 50µm. **See also Figure S6.**

Figure 6: Inhibition of metabolic reprogramming in either CAF or cancer cells blunts tumor progression. A) Following 67NR co-implantation with CAFs stably transfected with indicated doxyxycline inducible shRNA, mice were treated with doxyxycline (n=10 per group). **B)** Graphic representation of tumor formation induced by 67NR cells alone or in the presence of CAFs stably transfected with indicated shRNA. Total numbers of mice bearing tumors or invasive tumors after treatment are shown. **C)** Representative images of primary tumors isolated from mice (left panels) showing 67NR cells invading from the primary tumor (T) into the adjacent tissue (aT). Picrosirius red staining visualized by both parallel (upper panels) and orthogonal (middle panels) light display tumor ECM remodeling at the areas invaded by the tumoral 67NR cells. Representative IHC images show PCNA staining and the overall percentage of PCNA+ tumor cells. **D)** Following implantation of stably transfected 4T1 cells, mice were treated with doxycycline in order to induce inhibition of either GLS1 (n=10), SLC1A3 (n=10), or both GLS1 and SLC1A3 together (n=11). **E-H)** Tumor progression was assessed by the tumor volume (E), percentage of PCNA+ tumor cells (F), lung macro

metastasis number (G) and survival outcome (H). Each dot represents a mouse. **I)** Following 4T1 cells implantation, mice were treated with daily i.p. injections of CB839 (n=10); with daily i.p. injections of TFB-TBOA (n=10); with daily i.p. injections of both TFB-TBOA and CB839 (n=10) or vehicle (n = 10). **J-M)** Tumor progression was assessed by the tumor volume (J), lung macro metastasis number (K), survival outcome (L), and percentage of PCNA+ tumor cells (M). Each dot represents a mouse. Data are expressed as the mean ± SEM (*P < 0.05, **P < 0.01, ***P < 0.001). Group comparisons were performed by 1-way ANOVA and post-hoc Tukey's tests. Scale bars: 50µm. **See also Figure S7.**

Figure 7: Additive effects among pharmacological inhibitors of metabolic reprogramming in primary HNSCC tumors. A-D) Analysis of GLS1 (A) and SLC1A3 (C) mRNA levels in human head and neck squamous carcinoma tumors (HNSCC, n=497) and normal head and neck tissues (n=44). Kaplan-Meier survival analysis is shown for patients with HNSCC by log-rank test. Patients were divided by the expression levels of GLS (B) or SLC1A3 (D) mRNA. High expression: upper quartile (n=130); Low/medium expression: below the upper quartile (n=389). **E)** Representative images of primary HNSCC tumors are shown as isolated from a cohort of 48 patients stratified by their invasiveness score. Picrosirius red staining visualized by both parallel (upper panels) and orthogonal (middle panels) light displays tumor ECM remodeling, and representative IHC images show GLS1 (red) and SLC1A3 (gray) staining (lower panels). **F)** Quantification of collagen remodeling, GLS1, and SLC1A3 protein expression levels in low, middle, and high invasive HNSCC patients. **G-H)** Correlation between GLS staining and invasiveness and between SLC1A3 staining and invasiveness are shown. Pearson correlation coefficient (R^2) are indicated. **I-J)** Representative images are shown of patient-derived spheroids (PDS) treated 72h with the indicated drugs and quantification of the surrounding invasion (n=7 HNSCC patients; each dot represents a PDS ($n \geq 5$), while each color represents a single patient. **K-M)** In the HNSCC PDX mouse model, following tumor implantation, mice were treated with daily i.p. injections of CB839 (N=3; n=6); with daily i.p. injections of TFB-TBOA (N=3; n=6); with daily

i.p. injections of both TFB-TBOA and CB839 (N=3; n=6) or vehicle (N=3; n = 6). HNSCC progression was quantified by tumor volume (K) measurement, PCNA (red) staining (L) and overall percentage of PCNA+ tumors cells (M). Data are expressed as the mean ± SEM (*P < 0.05, **P < 0.01, ***P < 0.001). Paired samples were compared by 2-tailed Student's t test, while 1-way ANOVA and post-hoc Tukey's tests were used for group comparisons. Scale bars:100μm.

STAR* METHODS

- **CONTACT FOR REAGENT AND RESOURCE SHARING**

Further information and requests for resources and reagents should be directed to and will be fulfilled by Thomas BERTERO (bertero@unice.fr)

EXPERIMENTAL MODEL AND SUBJECT DETAILS

Cell Culture and cell culture reagents.

Human cancer cell lines including SCC12 (gift from Eric Sahai's lab), A549 (ATCC), MDA-MB-468 (ATCC) and human HEK293T (ATCC) cells as well as murine breast cancer cell lines 67NR (CAL, Cell Culture repository), 410.4 (CAL, Cell Culture repository) and 4T1 (ATCC) were maintained in DMEM supplemented with 10% FCS (fetal calf serum) and 2mM glutamine. Carcinoma associated fibroblasts (CAFs) were isolated from untreated head and neck, lung or breast tumors resected and considered de-identified 'surgical waste' tissues. Patients gave informed consent for tissue collection. Stromal cells that outgrew the cancer cells in culture were isolated by differential trypsinization. These cells were cultured in DMEM supplemented with 10% FCS, 2mM glutamine, 1% Pen/Strep and insulin-transferrin-selenium (Invitrogen). CAFs were verified by measuring Vimentin and α-SMA expression as well as by their ability to contract a collagen I rich gel in the absence of serum and to promote cancer cell invasion in 3D cell culture. CAFs from at least three different donors were randomly used throughout the experiments. All cells were grown in collagen-coated plastic (50ug/mL) at 37^{o}C in a humidified 5% CO_2 atmosphere. Experiments were performed at passages 2-10. All cells were routinely tested for mycoplasma by PCR and were carefully maintained in a centralized cell bank.

Balb/C CAF were generated from BALB/cAnNRj female mice (Janvier) harboring mouse breast carcinoma. These animals were injected with 5×10^5 4T1 cells into the mammary fat pad. Mammary tumors were resected at 3 weeks, digested in collagenase and dispase and mechanically minced. Cells were plated in cell culture dishes in DMEM (Gibco) with 10% FBS. Stromal cells that outgrew the cancer cells in culture were isolated by differential trypsinization. Cells were kept in DMEM (Gibco) with 10% FBS and 1% Pen/strep. CAFs

were verified by measuring Vimentin and α-SMA expression. CAFs in culture were frequently checked to confirm they were negative for EpCAM or CD31 and positive for α-SMA and vimentin.

Conditioned medium was generated by adding fresh medium to cells at > 50% confluence. Medium was harvested 48 h later and passed through 0.45-μm filters. Boiled medium experiments were performed by heating conditioned medium at 100 °C for 15 min followed by filtration at 0.45-μm to remove precipitate. Freeze-thaw medium was treated by 3 consecutive cycles of 15 min at − 80 °C followed by 15 min at 60 °C and then filtered to remove precipitate. In Figures 2 to 4 and Supplemental Figures 3 to 5, boiled conditioned medium was used.

Collagen-coated hydrogels were purchased from Matrigen.

The following inhibitors were used in this study: CB839 (Selleckchem), TFB-TBOA (Tocris) and Y27632 (Selleckchem) at 10 μM, Verteporfin (Sigma Aldrich) and PF573228 (Selleckchem) at 2 μM.

Glutamate was purchased from Sigma Aldrich and used at concentration of 5mM; aspartate was purchased from Sigma Aldrich and used at concentration of 5mM, consistent with prior *in vitro* studies linking cancer cell proliferation to glutamine metabolism and aspartate levels (Birsoy et al., 2015; Sullivan et al., 2015).

In vivo animal studies

All animal experiments were approved by the local committee of the host institute and by the Institutional Animal Care and Use Committee (CIEPAL AZUR committee, MESR number 2015051917125051) at the University Cote d'Azur, Nice, France. 8 weeks old female Balb/c mice and 8 weeks old female NMRI-nu (RjOrl:NMRI-Foxn1nu /Foxn1nu) mice were obtained from Janvier Laboratory. In all experiments, mice were randomly assigned to experimental groups.

Inhibition of YAP and Lox in breast cancer mouse model.

Metastatic mouse (Balb/c) 4T1 breast cancer cells (Yang et al., 2004) were implanted into the right fourth mammary fat pad in 10 µl Matrigel of 8-week-old female Balb/c mice. After 10 days, mice with palpable tumor (5-10mm^3) were randomly assigned to treatment groups and underwent i.p. injection daily with 20mg/kg of Verteporfin (Tocris Bioscience, UPS) or vehicle control. In a parallel but separate mouse cohort, β-aminopropionitrile (BAPN; 100 mg/kg/d; Sigma-Aldrich) was administered in drinking water. Tumor dimensions were measured using digital calipers, and tumor volume was calculated as (small diameter)^2 × (large diameter)/2. For survival analyses, mice were monitored daily for breast cancer progression and euthanized according to a standard body condition score, taking into account initial signs of moribund state and discomfort associated with the progression of breast cancer. Mice were also euthanized when total tumor burden exceeded 1,500 mm^3 in volume. Postmortem, the lungs and livers were harvested and examined for the presence of macroscopic lesions.

Genetic inhibition of GLS1 and/or SLC1A3 in 4T1 breast cancer mouse model

Metastatic mouse (Balb/c) 4T1 ($5x10^4$) breast cancer cell line stably transfected with either doxycycline inducible sh-NC (Control) or shGLS1 or shSLC1A3 or shGLS1 and shSLC1A3 were implanted into the right fourth mammary fat pad in 10 µl Matrigel of 8-week-old female Balb/c mice. After 11 days, mice with palpable tumor (5-10mm^3) were treated with 1mg/mL doxycycline (Sigma) 5% sucrose in drinking water. Tumor dimensions were measured using digital calipers, and tumor volume was calculated as (small diameter)^2 × (large diameter)/2. For survival analyses, mice were monitored daily for breast cancer progression and euthanized according to a standard body condition score, taking into account initial signs of moribund state and discomfort associated with the progression of breast cancer. Mice were also euthanized when total tumor burden exceeded 1,500 mm^3 in volume. Postmortem, the lungs were harvested and examined for the presence of macroscopic lesions.

Genetic inhibition of GLS1 and/or SLC1A3 in 67NR breast cancer mouse model

Non invasive mouse (Balb/c) 67NR ($5x10^5$) breast cancer cells were co-implanted with CAF ($1x10^6$) isolated from Balb/c mammary tumor and stably transfected with either doxycycline inducible sh-NC (Control) or shGLS1 or shSLC1A3 or shGLS1 and shSLC1A3 were implanted into the right fourth mammary fat pad in 10 µl Matrigel of 8-week-old female Balb/c mice. After 15 days, mice were treated with 1mg/mL doxycycline (Sigma) 5% sucrose in drinking water. Mice were killed 35 days post injection and tumors were removed. After excision and 12 h of fixation in 3.7% neutral-buffered formalin at 25 °C, tumors were paraffin-embedded. For invasion analyses, 5-µm paraffin sections were made and stained with haematoxylin and eosin or Picrosirius Red. Local invasion was determined by observation under light microscopy.

Pharmacological *inhibition of GLS1 and/or SLC1A1-3 in breast cancer mouse model.*

Metastatic mouse (Balb/c) 4T1 breast cancer cells were implanted into the right fourth mammary fat pad in 10 µl Matrigel of 8-week-old female Balb/c mice. After 10 days, mice with palpable tumor (5-10mm^3) were randomly assigned to treatment groups and underwent i.p. injection daily with 20mg/kg of CB839 (Tocris Bioscience) or with 20mg/kg of TFB-TBOA or with 20mg/kg CB839 and 20mg/kg TFB-TBOA or vehicle control. Tumor dimensions were measured using digital calipers, and tumor volume was calculated as (small diameter)^2 × (large diameter)/2. For survival analyses, mice were monitored daily for breast cancer progression and euthanized according to a standard body condition score, taking into account initial signs of moribund state and discomfort associated with the progression of breast cancer. Mice were also euthanized when total tumor burden exceeded 1,500 mm3 in volume. Postmortem, the lungs, and livers were harvested and examined for the presence of macroscopic lesions. After excision and 12 h of fixation in 3.7% neutral-buffered formalin at 25 °C, lungs were paraffin-embedded. For metastatic index calculation, 5-µm paraffin sections were made and stained with Picrosirius Red. Metastatic index was determined as described below (see Method detail section).

Generation of patient derived xenograft.

Tumor specimens were obtained at initial surgery (Face and Neck University Institute, Nice, France) from primary diagnosed HNSC. None of the patients received neoadjuvant chemotherapy or radiotherapy. Written informed consent was obtained from each patient and the study was approved by the hospital ethics committee. Patient tumor material was collected in culture medium and partially digested during 1 hour at room temperature in RPMI1640 with 1 mg/ml Collagenase IV, 1 mg/ml Dispase and 1 mg/ml Hyaluronidase. Approximately 20–30 mg tissue fragments in 50 % Matrigel were implanted subcutaneously into the flank region of NMRI-nu (RjOrl:NMRI-Foxn1nu /Foxn1nu) mice. The first passage PDX were dissociated in a collagenase/dispase mixture and cells were cultured in low serum conditions (2 %FBS/F12/DMEM/1XB27) in presence of 5 ng/ml EGF. Subsequently, $75x10^4$ cells in 50 % Matrigel were implanted subcutaneously into the flank region of NMRI-nu (RjOrl:NMRI-Foxn1nu /Foxn1nu) mice. One week after tumor engraftment, to avoid any interference with tumor uptake, mice were treated with the corresponding inhibitors. CB838 (20mg/kg), TFB-TBOA (20mg/kg) or a combination of CB839 (20mg/kg) and TFB-TBOA (20mg/kg) were injected intraperitoneally every day. Tumor volume was measured every day from the beginning of the treatment with the following formula: $(\text{small diameter})^2 \times (\text{large diameter})/2$.

Human studies.

All experimental procedures involving the use of human tissue included the relevant receipt of written informed consent and were approved by the institutional review board at Nice University Hospital. Ethical approval for this study and informed consent conformed to the standards of the Declaration of Helsinki. For formalin-fixed paraffin-embedded HNSCC samples, human specimens were collected from the Pasteur hospital tissues biobank and the protocol for staining was approved by the local ethics committee of the Nice University Hospital. All the observations on tumor samples were performed by independent double-blind examiners. The Quick Score method was used to score invasiveness of the tumor

samples by quantification of the number of invasive clusters within the tumor stroma. Tumor samples were classified for high, middle and low invasiveness corresponding to a QS <7, 8<QS<11 and 12<QS<16 respectively. GLS1, SLC1A3 and α-SMA staining were quantified on low, middle and high invasiveness samples as determined by measuring the mean value with imageJ software.

- **METHOD DETAILS**

Oligonucleotides and Transfection

On Target Plus siRNAs for YAP (J-012200-07 and J-012200-05,), TAZ (WWTR1; J-016083-05 and J-016083-06), GLS1 (J-004548-09; J-004548-10), SLC1A3 (J-007427-05; J-007427-07) and scrambled control D-001810-01 and D-001810-02) were purchased from ThermoScientific/Dharmacon. Cells were plated on collagen-coated plastic (50ug/mL) and transfected 24h later at 70-80% confluence using siRNA (25nM) and Lipofectamine 2000 reagent (Life Technologies), according to the manufacturers' instructions. Eight hours after transfection, cells were trypsinized and re-plated on hydrogel or used for spheroid assay.

Plasmids

The following antisense sequences: Control (CCGGCAACAAGATGAAGAGCACCAACTCGAGTTGGTGCTCTTCATCTTGTTGTTTTTG), Gls1 (CCGGAAGTTCCTTTTTGTCTTCAGTCTCG AGACTGAAGACAAAAAGGAACTTTTTTTG), and Slc1a3 (CCGGCTTTCAAGTTTTTGGTGT AACCTCGAGGTTACACCAAAAACTTGAAAGTTTTTG) were sub-cloned into pLKO-Tet-On (Wiederschain et al., 2009) using EcoRI and AgeI restriction sites. Stable expression of these constructs in 4T1 cells, and BalB/c mouse CAFs was achieved by lentiviral transduction. The YAP1 coding sequence was purchased (Addgene; Plasmid #18881) and sub-cloned in the pCDH-CMV-MCS-EF1-copGFP (System Biosciences) using EcoRI and NotI restriction sites. The lentiviral parent vector expressing GFP was

used as a control. The GLS1 coding sequence was purchased (Transomic technologies; BC038507) and sub-cloned in the pLJM1-EGFP Puromycin (Addgene; Plasmid #19319). The PMXS retroviral vector containing the coding sequence for SLC1A3 was purchased (Addgene; Plasmid #72873). All cloned plasmids were confirmed by DNA sequencing.

Lentivirus production

HEK293T cells were transfected using Lipofectamine 2000 (Life Technologies) with lentiviral plasmids along with packaging plasmids (pPACK, System Biosciences), according to the manufacturer's instructions. Virus was harvested, sterile filtered (0.45-μm), and utilized for subsequent infection of 4T1 and Balb/c mouse CAFs (24-48 hour incubation), and for SCC12 and CAFs (24-48 hour incubation) for gene transduction.

Extracellular flux analyses.

SCC12 (20,000 cells per well) or CAFs (5,000 cells per well) were plated in Seahorse Bioscience 24-well plates precoated with 20 μl of soft or stiff gel (as described above). After overnight incubation to allow attachment, cells were washed 2 times in assay medium (DMEM without phenol red or pyruvate containing 0.5% dialyzed FBS, 2mM Glutamine and 0.1 mg/ml uridine at pH 7.4; Seahorse Biosciences) and incubated in 500 μl of fresh assay medium. Oxygen consumption rate and extracellular acidification rate (a surrogate marker of glycolysis) were measured on an XFe24 Analyzer (Seahorse Biosciences). Mitochondrial and glycolytic stress assays were performed according to the manufacturer's protocols. Oxygen consumption rate and extracellular acidification rate were normalized to cell count measured after assay completion.

Medium metabolite measurements

For kinetics of metabolite secretion by CAF or SCC12, triplicate samples of subconfluent CAF or SCC12 cultured under soft (1kPa) or stiff (8kPa) condition were changed to fresh

DMEM with 10% FBS, which was allowed to condition for 48 h. Metabolites were then extracted from conditioned medium by adding ice cold 100% MeOH to a final concentration of 80% MeOH. Medium collected from cell-free plates after 48 h incubation was used as the baseline control to calculate the consumption or production of each metabolite, which was further normalized by the proliferation rate. . The cell numbers were measured from duplicate treatment plates to determine the proliferation rate, and the metabolite flux was determined with the following formula:

Uptake/secretion rate = Δ metabolite / (Δ time * average cell number)

Average cell number = Δ cell number / (growth rate* Δ time)

Uptake/secretion rate = (Δ metabolite / Δ time) * (growth rate * Δ time / Δ cell number) = (Δ metabolite / Δ cell number) * growt rate

Growth rate [1/h] = LN (cell number T1) – LN (cell number T0) / time (T1)- time (T0)

Cell-cell metabolite transfer measurements

For SCC12 metabolite uptake kinetics, conditioned DMEM with 10% FBS from subconfluent CAF or SCC12 was collected after 48 h of culture, and then filtered through a 0.45-μm filter. SCC12 cells were plated in triplicate and treated with the CAF-CM or SCC12 CM for 24 h. The medium was removed and the cell lysate harvested with ice cold 80% MeOH. The soluble metabolite fractions were cleared by centrifugation, dried under nitrogen, then resuspended in 50:50 MeOH:H2O mixture for LC–MS analysis.

For CAF metabolite uptake kinetics conditioned DMEM with 10% FBS from subconfluent CAF or SCC12 was collected after 48 h of culture, and then filtered through a 0.45-μm filter. CAF cells were plated in triplicate and treated with the CAF-CM or SCC12-CM for 24h. The medium was removed and the cell lysate harvested with ice cold 80% MeOH. The soluble metabolite fractions were cleared by centrifugation, dried under nitrogen, then resuspended in 50:50 MeOH:H2O mixture for LC–MS analysis.

Targeted LC-MS

Metabolite extraction was performed essentially as described with minor modifications (Bertero et al., 2016; Oldham et al., 2015). Briefly, metabolites were extracted from cultured cells on dry ice using 80% aqueous methanol precooled at –80°C. Supernatants were extracted with 4 volumes of 100% methanol precooled at –80°C for 4 hours at –80°C. An internal standard, [$^{13}C_4$]-2-oxoglutarate ([13C4]-2OG) (Cambridge Isotope Laboratories), was added during metabolite extraction. Insoluble material from both cell and supernatant extractions was removed by centrifugation at 20,000 g for 15 minutes at 4°C. The supernatant was evaporated to dryness by SpeedVac at 42 °C, the pellet was resuspended in LC-MS water, and metabolites were analyzed by LC-MS.

LC-MS analysis was performed on a Vanquish ultra-high performance liquid chromatography system coupled to a Q Exactive mass spectrometer (Thermo) that was equipped with an Ion Max source and HESI II probe. External mass calibration was performed every seven days. Metabolites were separated using a ZIC-pHILIC stationary phase (150 mm × 2.1 mm × 3.5 mm; Merck) with guard column. Mobile phase A was 20 mM ammonium carbonate and 0.1% ammonium hydroxide. Mobile phase B was acetonitrile. The injection volume was 1 μL, the mobile phase flow rate was 100 μL/min, the column compartment temperature was set at 25 °C, and the autosampler compartment was set at 4 °C. The mobile phase gradient (%B) was 0 min, 80%; 5 min 80%; 30 min, 20%; 31 min, 80%; 42 min, 80%. The column effluent was introduced to the mass spectrometer with the following ionization source settings: sheath gas 40, auxillary gas 15, sweep gas 1, spray voltage +/- 3.0 kV, capillary temperature 275 °C, S-lens RF level 40, probe temperature 350 °C. The mass spectrometer was operated in polarity switching full scan mode from 70-1000 m/*z*. Resolution was set to 70,000 and the AGC target was $1x10^6$ ions. Data were acquired and analysed using TraceFinder software (Thermo) with peak identifications based on an in-house library of authentic metabolite standards previously analysed utilizing this method. For all metabolomic experiments, the

quantity of the metabolite fraction analysed was adjusted to the corresponding cell number calculated upon processing a parallel experiment.

^{13}C tracing experiments

To trace the effect of glucose or glutamine on amino acid and glucose metabolism, CAFs or SCC12 cells were grown 48h on 1kPa hydrogel or 8kPa hydrogel in DMEM containing 10% FBS, 4.5g.L^{-1} glucose, 2mM glutamine and then transferred into glucose-free (with 2 mM glutamine) or glutamine free (with 4.5g.L^{-1} glucose) DMEM containing 10% dialyzed FBS and supplemented with either 4.5g.L^{-1} U-^{13}C-glucose or 2mM U-^{13}C-glutamine, respectively overnight. To trace aspartate metabolism, SCC12 cells were grown as above and then transferred into DMEM (with 4.5g.L^{-1} glucose, 2 mM glutamine, 10% dialyzed FBS) and supplemented with 5 mM ^{13}C-aspartate overnight. To trace glutamate metabolism, CAFs were grown as above and then transferred into DMEM (with 4.5g.L^{-1} glucose, 2 mM glutamine, 10% dialyzed FBS) and supplemented with 5 mM ^{13}C-glutamate overnight.

Analysis of intracellular amino acids was performed as described previously(Heuillet et al., 2018). Briefly, analysis was performed by liquid chromatography (HPLC U3000, Dionex, Sunnyvale, CA, USA) coupled with a LTQ Orbitrap Velos mass spectrometer (Thermo Fisher Scientific, Waltham, MA, USA) equipped with a heated ESI probe. MS analyses were performed in the positive FTMS mode at a resolution of 60,000 (at m/z 400) with the following source parameters: capillary temperature was 275 °C, source heater temperature was 250 °C, sheath gas flow rate was 45, auxiliary gas flow rate was 20, S-Lens RF level was 40%, and source voltage was 5 kV. Samples were injected on a Supelco HS F5 Discovery column (150 mm × 2.1 mm; 5 µm particle size) equipped with a Supelco HSF5 guard column (20 mm × 2.1 mm; 5 µm particle size). Solvent A was 0.1% formic acid in H2O and solvent B was 0.1% formic acid in acetonitrile at a flow rate of 250 µL.min−1. The solvent B was varied as follows: 0 min: 2%, 2 min: 2%, 10 min: 5%, 16 min: 35%, 20 min: 100%, 24 min: 100%, 24.1min: 2% and 30 min: 2%. The volume of the injection was 20 µL.

Identification was determined by extracting the accurate mass of amino acids with a mass accuracy of 5 ppm.

Analysis of intracellular central metabolites was performed by high performance anion exchange chromatography (Dionex ICS 5000+ system, Sunnyvale, USA) coupled with a LTQ Orbitrap Velos mass spectrometer (Thermo Fisher Scientific, Waltham, MA, USA) equipped with a heated ESI probe. Samples were analyzed in the negative FTMS mode at a resolution of 60,000 (at m/z 400) with the following source parameters: capillary temperature was 300°C, source heater temperature was 250 °C, sheath gas flow rate was 30, auxiliary gas flow rate was 10, S-Lens RF level was 50%, and source voltage was 2,5 kV. The injection volume was 5 µL. Samples were injected on a Dionex IonPac AS11 column (250 x 2mm) equipped with a Dionex AG11 guard column (50 x 2mm). Mobile phase was composed of a KOH gradient which varied as follows: 0min 0,5; 1min 0,5; 9.5min 4,1; 14.6min 4.1; 24min 9.65; 36min 60; 36.1min 90; 43min 90; 43.1min 0,5; 45min 0.5.

Isotopic cluster of each amino acids and central metabolites was determined by extracting and integrating the exact mass of all 13C-isotopologues with Tracefinder® software (Thermo Fisher Scientific). The correction of this data for naturally occurring isotopes other than carbon to extract carbon isotopologues was performed with IsoCor® adapted for higt resolution mass spectrometry (Millard et al., 2012). The Carbon Isotopologues Distributions (CIDs) were calculated from the corrected area of each isotopologue constituting the isotopic clusters. CIDs were expressed relative to the sum of all analyte isotopologues.

$^{13}C_5$-glutamine, $^{13}C_5$-glutamate and $^{13}C_4$-aspartate were purchased from Sigma-Aldrich while $^{13}C_6$-glucose was purchased from Cambridge Isotope Laboratories.

Measurements of metabolite levels by kits

The levels of selected metabolites were measured by commercial kits to confirm the results of metabolic profiling. These include the aspartate colorimetric assay kit (BioVision), the

glutamate colorimetric assay kit (BioVision), the glutamine colorimetric assay kit (BioVision), the glucose colorimetric assay kit (BioVision), the lactate colorimetric assay kit (BioVision) the NAD+/NADH assay kit (Sigma-Aldrich), and the GSH/GSSG colorimetric assay kit (Abcam) The manufacturers' protocols were followed. Cell number was determined in concurrent experiment run in parallel, averaged per condition, and the metabolite consumption/production rates were calculated per cell.

Messenger RNA extraction

Cells were homogenized in 1 ml of QiaZol reagent (Qiagen). Total RNA content was extracted using the miRNeasy kit (Qiagen) according to the manufacturer's instructions. Total RNA concentration was determined using a ND-1000 micro-spectrophotometer (NanoDrop Technologies).

Quantitative RT-PCR of messenger RNAs

Messenger RNAs were reverse transcribed using the Multiscript RT kit (Life Technologies) to generate cDNA. cDNA was amplified via fluorescently labeled Taqman primer sets using an Applied Biosystems 7900HT Fast Real Time PCR device. Fold-change of RNA species was calculated using the formula ($2^{-\Delta\Delta Ct}$), normalized to RPLP0 expression.

Matrix remodeling assay.

For gel contraction assay, $25x10^3$ cells were embedded in 100µl of matrix gel and seeded in triplicate into 96 wells plate. After 1h at 37°C, matrix gels were overlaid with 100µl of 0.5% FCS medium (with indicated cytokines or inhibitors) and changed every two days. At day 6 the relative diameter of the well and the gel were measured using ImageJ. The percentage of gel contraction was calculated using the formula 100 * (well diameter – gel diameter) / well diameter.

Traction force microscopy.

Contractile forces exerted by CAF on different stiffness gels were assessed by traction force microscopy essentially as described (Liu et al., 2016). Briefly, polyacrylamide substrates with shear moduli of 1, or 8 kPa conjugated with fluorescent ed latex microspheres (0.5 μm, 505/515 ex/em) were purchased from Matrigen. CAF were plated on fluorescent bead–conjugated discrete stiffness gels and grown for 24 hours, at which time they were treated with the indicated treatments for 1 hour before traction force measurements. Images of gel surface–conjugated fluorescent beads were acquired for each cell before and after cell removal using a Axiovert 200M motorized microscope stand (Zeiss) and a ×32 magnification objective. Tractions exerted by CAF were estimated by measuring bead displacement fields, computing corresponding traction fields using Fourier transform traction microscopy, and calculating root-mean-square traction using the PIV 5particle Image velocity) and TFM (Traction force microscopy) pakage on ImageJ (Tseng et al., 2012). To measure baseline noise, the same procedure was performed on a cell-free region.

Magnetic Bead Force Assays

The application of tensile force to integrins using magnetic beads was performed as previously described. In brief, paramagnetic beads (Dynabeads, Invitrogen) were coated with Collagen I (Bays et al., 2014). The beads were incubated with cells for 40 min at 37°C. Tensile forces were applied to beads for the indicated times using a permanent magnet. For all experiments, the magnet was placed parallel to and at a distance of 0.6 cm from the cell surface, so that the force on a single bead was approximately 10 pN (Bays et al., 2014; Guilluy et al., 2011). After application of force, the cells were transferred to ice and immediately fixed/lysed for immunofluorescence/RT-qPCR analyses.

Cell counting assays.

SCC12 cells transfected or not with the indicated siRNA were plated in triplicate in 6 well plates at 30,000 cells per well. After overnight incubation for cells to adhere, 6 wells were counted to determine initial count at the time of treatments (glutamate, aspartate, CB-839 or

TFB-TBOA). After 1 day, 2 days or 3 days, the entire contents of the well were trypsinized and counted and proliferation rate was calculated.

Proliferation assays

SCC12 cells transfected or not with the indicated siRNA were plated in triplicate in 24-well glass-bottomed hydrogel cell culture plates (Matrigen) at 5,000 cells per well. After overnight incubation for cells to adhere, 24 wells were treated with the indicated CM for 24h. Ki67 immunolabeling was performed as described below. Images were obtained using an Olympus Bx51 microscope or ZEISS LSM Exciter confocal microscope. Percentage of Ki67+ cells was determined and at least four 20x field per condition were averaged together.

Three-dimensional co-culture invasion assay

Spheroid assay was performed as we described before (Albrengues et al., 2013; Gaggioli et al., 2007). Briefly, cancer cells (SCC12 or MDA-MB-468) and CAF cells were removed from the cell culture dishes with trypsin and re-suspended in DMEM 10% FCS. The solution contained a 1:1 ratio of cancer cells and CAF cells at a concentration of 1×10^6 cells per mL. Fifty-microliter droplets were plated onto the underside of a 10 cm culture dish and allowed to form spheroids in a 37 °C incubator for 24 hours. The spheroids were then embedded in a collagen I/Matrigel gel mix at a concentration of approximately 4 mg/ml collagen I and 2 mg ml−1 Matrigel (BD Bioscience) in 24-well glass-bottomed cell culture plates (MatTek). The gel was incubated for at least 45 min at 37 °C with 5% CO2. The gel was covered with DMEM media. Forty-eight hours later, the spheroids were imaged with an inverted microscope at a magnification of 4x and 10x. Invasion was quantified using ImageJ.

Immunoblotting and antibodies

Cells were lysed in Laemmeli buffer. Protein lysates were resolved by SDS-PAGE and transferred onto a PVDF membrane (Biorad). Membranes were blocked in 5% non-fat milk in TN buffer (50 mM Tris-HCl pH 7.4, 150 mM NaCl) or 5% BSA in TN buffer and incubated in

the presence of the primary and then secondary antibodies. After washing in TN buffer containing 0.1% Tween, immunoreactive bands were visualized with the ECL system (Amersham Biosciences). Primary antibody for YAP1 (#4912; 1/1000) and YAP/TAZ (#8418; 1/1000) were obtained from Cell Signaling. Primary antibodies for GLS1 (ab156876; 1/1000), and LDHA (ab47010; 1/1000) were obtained from Abcam. Primary antibody for Tubulin (T4026; 1/5000) was obtained from Sigma Aldrich. Primary antibody for SLC1A3 (sc-7757; 1/200) was obtained from Santa Cruz Biotechnology. Appropriate secondary antibodies (anti-rabbit, anti-mouse and anti-goat) coupled to HRP were used (Dako).

Immunofluorescence

After the different treatment cells were fixed with PBS/PFA 4% for 10 min and permeabilized with PBS/Triton 100X 0.1% for 10min. Then cells were incubated with anti-PCNA (#4912; 1/100; Invitrogen) or anti-YAP (#14074S; 1/100; Cell signalling) or anti-Ki67 (ab15580; 1/300; Abcam) at room temperature for 2 hours. Secondary antibodies coupled with Alexa-594 (Thermo Scientific) were used at 1:500. F-actin was counterstained with Alexa-488 Phalloidin (Thermo Scientific). Nuclei were counterstained with DAPI (Sigma-Aldrich). Pictures were obtained using a ZEISS LSM Exciter confocal microscope.

Glutaminase activity assay

According to the manufacturer instructions (Glutaminase Microplate Assay Kit, Cohesion Biosciences), flash frozen tissue (0.1g/sample) or cells ($1x10^6$ cells) was homogenized in 1mL of assay buffer on ice and centrifuged at 8000g 4°C for 10 min. Protein concentration was determined by Bradford assay. Samples, normalized to total protein (100µg) or cell numbers, were incubated with kit reagents for 1 hr at 37°C, and absorbances were measured at 420nm.

GDH activity assay.

According to the manufacturer instructions (Glutamate Dehydrogenase Activity Assay kit, Abcam, ab102527), cells (1.10^6 cells) were homogenized in 200µL of assay buffer on ice and centrifuged at 13 000g 4°C for 10 min. Protein concentration was determined by Bradford assay. Samples, normalized to total protein (100µg), were incubated with kit reagents for 1 hr at 37°C, and absorbances were measured at 450nm.

LOX activity assay

Lox activity was measured using the Lysyl Oxidase Activity Assay Kit (Abcam; Ab112139), following the manufacturer instructions and as we previously described. Briefly, 5µg of total protein extracts from whole tumor, as described above, were analyzed. Extracts were incubated for 30min in presence of 50uL of reaction mixture +/- 500µM BAPN. Fluorescence was monitored with a fluorescence plate reader at Ex/Em = 540/590 nm and fluorescence (a measure of LOX activity) was plotted, where 0 = sample + 500µM BAPN (complete LOX inhibition).

Immunohistochemical staining and quantification methods of human samples.

48 head and neck tumor biopsies were fixed (3.7% formaldehyde in PBS) for 4 h and transferred to 70% ethanol (24 h), embedded in paraffin wax and sectioned at 5 µm. After deparaffinization and rehydration, microwave antigen retrieval was performed in Na-citrate buffer (10mM, pH6; 5min at 900W, 10min at 150W and 30 min at room temperature). Sections were washed three times in PBS (5min per wash). After incubation in blocking buffer for one hours (PBS 3%BSA; 10% serum; 0.3% Triton X100), sections were incubated with primary antibody for α-SMA (ab21027; 1/300), SLC1A3 (sc-7757; 1/100) and GLS1 (ab156876; 1/100) staining diluted in blocking buffer overnight at 4°C. After three washes in PBS/0,1% Tween 20, sections were incubated with secondary antibody diluted 1:400 in blocking buffer for 1 hour at room temperature and washed 3 times in PBS/0,1% Tween 20. Nuclei were then stained with DAPI and mounted in Permafluor (Thermo Scientific). Two authors, blinded to each other's assessment, scored the slides using the Quick Score

method (as described in (Albrengues et al., 2014) to determine SLC1A3, GLS1, and α-SMA status within the tumor.

Immunohistochemistry and immunofluorescence of mammary tumor sections

Mammary tumor sections (5µm) were deparaffinized and high temperature antigen retrieval was performed, followed by blocking in TBS/BSA 5%, 10% donkey serum and exposure to primary antibody and biotinylated secondary antibody (Vectastain ABC kit, Vector Labs) for immunohistochemistry or Alexa 488, 568 and 647-conjugated secondary antibodies (Thermo Fisher Scientific) for immunofluorescence. Primary antibodies against, GLS1 (ab93434; 1/100) and α-SMA (ab32575; 1/1000 or ab21027; 1/300) were purchased from Abcam. A primary antibody against α-SMA (A2547; 1/300) was purchased from Sigma. A primary antibody against SLC1A3 (sc-7757; 1/100), was purchased from Santa Cruz Biotechnology. A primary antibody against PCNA (13-3900, 1/100) was purchased from Thermo Fisher Scientific. In most cases, color development was achieved by adding streptavidin biotinylated alkaline phosphatase complex (Vector Labs) followed by Vector Red alkaline phosphatase substrate solution (Vector Labs). Levamisole was added to block endogenous alkaline phosphatase activity (Vector Labs). Pictures were obtained using an Olympus Bx51 microscope or ZEISS LSM Exciter confocal microscope. Intensity of staining was quantified using ImageJ software (NIH). All measurements were performed blinded to condition

Metastatic index calculation

To establish a metastatic index based on visual counting of lesions in the lungs, the excised lung fixed and embedded in paraffin were sectioned and stained with hematoxylin and eosin (H&E). Metastasis was quantified by determining the total tissue area per section (D1) and metastasis present in the same area (D2) using a reference grid. The metastatic index is calculated by the ratio D2/D1. At least three sections of whole lungs per sample separated by 100µm were averaged. A full picture of the lungs was obtained using a ZEISS high-

throughput microscope that allows the automated acquisition of large numbers of wide-field pictures. Image reconstitution was performed using the AxioVision® software. Surface areas were determined using Image J software (NIH).

Atomic force microscopy

Mice tumors were embedded in OCT, frozen on liquid nitrogen vapor and store at -80°C. Tumor slices (10 µm thickness) were cut from their glass slide and the fragment of glass containing the sample was glued on the bottom of a 50 mm dish (Willco Glass Bottom Dish). Before measurements the sample was first rinsed and covered with 4 ml of PBS 1x. The mechanical properties of the samples were studied using a BioScope Catalyst atomic force microscope (Bruker) coupled with and optical microscope (Leica DMI6000B) that enables, by phase contrast, to pinpoint the areas of interest. For each sample, at least 3 areas were analyzed using the "Point and Shoot" method, collecting from 80 to 100 force-distance curves at just as many discrete points. The experiments of nanoindentation were performed in PBS using a probe with a Borosilicate Glass spherical tip (5 µm of diameter) and a cantilever with a nominal spring constant of 0.06 N/m (Novascan). Indentations were carried out using a velocity of 6.5 µm/s, in relative trigger mode and by setting the trigger threshold to 2 nN. The apparent Young's (elastic) modulus was calculated using the NanoScope Analysis 1.8 software (Bruker), fitting the force curves to the Hertz spherical indentation model and using a Poisson's ratio of 0.5. To avoid large indentation, a minimum and a maximum Force Fit Boundary of 5% and 25% respectively of the whole force curve was taken into account for the fit.

Picrosirius red stain and quantification

Picrosirius red stain was achieved through the use of 5µm paraffin sections stained with 0.1% Picrosirius red (Direct Red80, Sigma-Aldrich) and counterstained with Weigert's hematoxylin to reveal fibrillar collagen. The sections were then serially imaged using with an

analyzer and polarizer oriented parallel and orthogonal to each other. Microscope conditions (lamp brightness, condenser opening, objective, zoom, exposure time, and gain parameters) were constant throughout the imaging of all samples. A minimal threshold was set on appropriate control sections for each experiment in which only the light passing through the orthogonally-oriented polarizers representing fibrous structures (*i.e.*, excluding residual light from the black background) was included. The threshold was maintained for all images across all conditions within each experiment. The area of the transferred regions that was covered by the thresholded light was calculated and at least five 20x field per condition were averaged together (Image J software).

Patient-derived spheroids

Following excision biopsy samples were directly transferred to freshly prepared culture medium containing DMEM/F12-medium, 10 % fetal calf serum, as well as a mixture of antibiotic/antifungal compounds (0.26 µM Amphotericin B, Ampicillin 0.14 mM, Ciprofloxacin 7.54 µM). Fresh tumor tissue samples were mechanically and enzymatically (Collagenase 200µg/mL in PBS; Roche) digested to generate a single-cell suspension. After determination of cell viability using the trypan-blue exclusion test, the single cell suspension was directly processed into spheroids. No red blood cell lysis was performed. Briefly, 50 uL droplets containing 25-50x10^3 cells were plated onto the underside of a 10 cm culture dish and allowed to form spheroids in a 37 °C incubator 48 hours. The spheroids were then embedded in a collagen I/Matrigel gel mix at a concentration of approximately 4 mg /ml collagen I and 2 mg/ml Matrigel (BD Bioscience) in 24-well glass-bottomed cell culture plates (MatTek). The gel was incubated for at least 45 min at 37 °C with 5% CO2. The gel was covered with DMEM/F12 media. Forty-eight hours later, the spheroids were imaged with an inverted microscope at a magnification of 4x and 10x. Invasion was quantified using ImageJ. Importantly, at the end of the experiments, patient-derived spheroids were analyzed (n=5 randomly chosen) to determine the presence of both cancer cells and CAFs. After 30mn fixation in 3.7% neutral-buffered formalin at 25 °C, PDS were paraffin-embedded. 5-µm

paraffin sections were stained for α-SMA, vimentin, and E-Cad. Confocal imaging revealed the presence of both cancer cells (E-Cad+, Vim-, α-SMA- cells and Ecad+, Vim+, α-SMA- cells) and CAF (α-SMA/vimentin double positive cells).

- **QUANTIFICATION AND STATISTICAL ANALYSIS**

Cell culture experiments were performed at least three times and at least in triplicate for each replicate. The number of animals in each group was calculated to measure at least a 20% difference between the means of experimental and control groups with a power of 80% and standard deviation of 10%. The number of unique patient samples for this study was determined primarily by clinical availability. *In situ* expression/histological analyses of both mouse and human tissue were performed in a blinded fashion. Numerical quantifications for *in vitro* experiments using cultured cells or *in situ* quantifications of transcript expression represent mean ± standard deviation (SD). Numerical quantifications for physiologic experiments using mouse or human reagents represent mean ± standard error of the mean (SEM). Immunoblot images are representative of experiments that have been repeated at least three times. Micrographs are representative of experiments in each relevant cohort. Paired samples were compared by a 2-tailed Student's *t* test for normally distributed data, while Mann-Whitney U non-parametric testing was used for non-normally distributed data. For comparisons among groups, one-way ANOVA and *post-hoc* Tukey testing was performed. A P-value less than 0.05 was considered significant. Correlation analyses were performed by Pearson correlation coefficient calculation. The Mantel-Cox log-rank test was used for statistical comparisons in survival analyses. No samples/animals/patients were excluded.

- **KEY RESOURCES TABLE**

REAGENT or RESOURCE	SOURCE	IDENTIFIER
Antibodies		
Rabbit monoclonal anti-GLS1	Abcam	ab156876
Rabbit polyclonal anti-GLS1	Abcam	ab93434

Rabbit polyclonal anti-LDHA	Abcam	ab47010
Rabbit polyclonal anti-Ki67	Abcam	ab15580
Goat polyclonal anti-αSMA	Abcam	ab21027
Rabbit monoclonal anti-αSMA	Abcam	ab32575
Goat polyclonal anti-SLC1A3	Santa Cruz Biotechnology	sc-7757
Rabbit polyclonal anti-YAP1	Santa Cruz Biotechnology	sc15407X
Rabbit monoclonal anti-YAP/TAZ	Cell Signaling Technology	#8418S
Rabbit monoclonal anti-YAP	Cell Signaling Technology	#14074S
Mouse monoclonal anti-P-MLC2	Cell Signaling Technology	#3675S
Mouse monoclonal anti-Tubulin	Sigma-Aldrich	T9026
Mouse monoclonal anti-αSMA	ThermoFisher Scientific	# MA5-11547
Mouse monoclonal anti-PCNA	ThermoFisher Scientific	# MA5-11358
Biological Samples		
Human Head and Neck Squamous Carcinoma blocks	Nice University Hospital pasteur tissues biobank	https://extranet.chu-nice.fr/prod-tumo/prod-tumo-fr/
Patient-derived spheroids (PDS)	Face and Neck University Institute Department of Oncologic Surgery, Nice	http://www.centreantoinelacassagne.org/institut-universitaire-de-face-coup/
Patient-derived xenografts (PDX)	Centre Antoine Lacassagne Cell Culture and Xenograft Repository	http://ircan.org/
Chemicals, Peptides, and Recombinant Proteins		
CB839 glutaminase inhibitor	Selleck Chemicals	S76655
Y27632 ROCK inhibitor	Selleck Chemicals	S1049
PF573228 FAK inhibitor	Selleck Chemicals	S2013
TFB-TBOA EAAT1/2/3 inhibitor	Tocris	2532
Verteporfin YAP inhibitor (*In vivo*)	USP	1711461
Verteporfin YAP inhibitor (*In vitro*)	Sigma-Aldrich	SML0534
BAPN lysyl-oxidase inhibitor	Sigma-Aldrich	A3134
L-Aspartic acid	Sigma-Aldrich	A7219
L-Glutamic acid	Sigma-Aldrich	G1251
L-Aspartic acid $^{13}C_4$	Sigma-Aldrich	604852
L-Glutamic acid $^{13}C_5$	Sigma-Aldrich	604860
L-Glutamine $^{13}C_5$	Sigma-Aldrich	605166
U$^{13}C_6$-Glucose	Cambridge Isotop Laboratories	CAS#110187
Critical Commercial Assays		
Aspartate colorimetric assay kit	BioVision	K552
Glucose colorimetric assay kit	BioVision	K606
Glutamate colorimetric assay kit	BioVision	K629
Glutamine colorimetric assay kit	BioVision	K556
Lactate colorimetric assay kit	BioVision	K607
Glutaminase microplate assay kit	Cohesion Bioscience	CAK1065
NAD/NADH quantification kit	Sigma-Aldrich	MAK037
Cellular ROS/Superoxide detection assay kit	Abcam	ab139476
Glutamate dehydrogenase activity assay kit	Abcam	ab102527
GSH/GSSG Ratio detection assay kit	Abcam	ab138881

LysylOxidase Activity assay kit	Abcam	ab112139
Experimental Models: Cell Lines		
Human: MDA-MB468 cell line	ATCC	HTB-132
Human: A549 cell line	ATCC	CCL-185
Human: SCC12 cell line	Eric Sahai Laboratory	CVCL_4026
Human:HEK293T	ATCC	CRL-3216
Human: HNSC-CAFs	This paper	N/A
Human: Breast-CAFs	This paper	N/A
Human Lung-CAFs	This paper	N/A
Mouse: 67NR cell line	Centre Antoine Lacassagne Cell Culture and Xenograft Repository	CVCL_9723
Mouse: 410.4 cell line	Centre Antoine Lacassagne Cell Culture and Xenograft Repository	CVCL_W343
Mouse: 4T1 cell line	ATCC	CRL-2539
Mouse: Brest-CAFs	This paper	N/A
Experimental Models: Organisms/Strains		
Mouse: BALB/cAnNRj	Janvier Labs	
Mouse: Rj:NMRI-Foxn1nu/nu	Janvier Labs	
Oligonucleotides		
siRNA GLS1_1: AAGTTCCCTTCTGTCTTCAGT	Dharmacon	J-004548-09
siRNA GLS1_2: AATGGTGGTTTCTGCCCAATT	Dharmacon	J-004548-10
siRNA SLC1A3_1:	Dharmacon	J-007427-05
siRNA SLC1A3_2:	Dharmacon	J-007427-07
siRNA YAP_1: GGUCAGAGAUACUUCUUA	Dharmacon	J-012200-05
siRNA YAP_2: GAACAUAGAAGGAGAGGAG	Dharmacon	J-012200-07
siRNA TAZ_1: GACAUGAGAUCCAUCACUA	Dharmacon	J-016083-05
siRNA TAZ_2: GGACAAACACCCAUGAACA	Dharmacon	J-016083-06
siRNA negative control_1: N/A	Dharmacon	D-001810-01
siRNA negative control_2: N/A	Dharmacon	D-001810-02
shRNA-Control target sequence: CCGGC**AACAAGATGAAGAGCACCAA**CTCGAG**TTGGTGCTCTTCATCTTGTTG**TTTTTG	This paper	N/A
shRNA Gls1 target sequence : CCGG**AAGTTCCTTTTTGTCTTCAGT**CTCGAG**ACTGAAGACAAAAAGGAAC**TTTTTTTG	This paper	N/A
shRNA Slc1a3 target sequence : CCGG**CTTTCAAGTTTTTGGTGTAAC**CTCGAG**GTTACACCAAAAACTTGAAAG**TTTTTG	This paper	N/A
Primer for ChIP-qPCR in Fig4J-K are listed in Sup Table 1	This paper	N/A
CTGF (Hs00170014_m1)	ThermoFisher Scientific	Cat#4331182
CYR61 (Hs00155479_m1)	ThermoFisher Scientific	Cat#4331182
GAPDH (Hs02758991_g1	ThermoFisher Scientific	Cat#4331182
GDH/GLUD1 (Hs03989560_s1)	ThermoFisher Scientific	Cat#4331182
GLS (Hs01014020_m1)	ThermoFisher Scientific	Cat#4331182
GOT1 (Hs00157798_m1)	ThermoFisher Scientific	Cat#4331182
LDHA (Hs00855332_g1)	ThermoFisher Scientific	Cat#4331182

SLC1A3 (Hs00904823_g1	ThermoFisher Scientific	Cat#4331182
SLC1A5 (Hs01056542_m1)	ThermoFisher Scientific	Cat#4331182
RPLP0 (Hs99999902_m1)	ThermoFisher Scientific	Cat#4331182
Ctgf (Mm01192933_g1)	ThermoFisher Scientific	Cat#4331182
Cyr61 (Mm00487498_m1)	ThermoFisher Scientific	Cat#4331182
Gls (Mm01257297_m1)	ThermoFisher Scientific	Cat#4331182
Ldha (Mm01612132_g1)	ThermoFisher Scientific	Cat#4331182
Slc1a3 (Mm00600697_m1)	ThermoFisher Scientific	Cat#4331182
Rplp0 (Mm01974474_gH)	ThermoFisher Scientific	Cat#4331182
Recombinant DNA		
pLKO-Tet-On Puromycin	Wiederschain et al., 2009	Addgene Plasmid #21915
pLKO-Tet-On Neomycin	Wiederschain et al., 2009	Addgene Plasmid #21916
pLJM1-EGFP Puromycin	Sancak et al., 2008	Addgene Plasmid #19319
pCDH-CMV-MCS-EF1-copGFP	System biosciences	CD511B-1
packaging plasmids (pPACK)	System biosciences	LV510A-1
cDNA GLS : BC038507	Transomic technologies	BC038507
pcDNA Flag Yap1	Levy et al., 2008	Addgene; Plasmid #18881
Mouse Slc1a3: pLKO mouse shRNA Slc1a3	This paper	N/A
Mouse Gls1: pLKO mouse shRNA Gls1	This paper	N/A
Human: pCDH-CMV-MCS-EF1-copGFP YAP1	This paper	N/A
Human: pLJM1-EGFP Puromycin GLS1	This paper	N/A
Human: PMXS-SLC1A3	Birsoy et al., 2015	Addgene; Plasmid #72873
Software and Algorithms		
GraphPad Prism 6	GraphPad software	https://www.graphpad.com/scientific-software/prism/
Image J	NIH	https://imagej-nih-gov.gate2.inist.fr/ij/

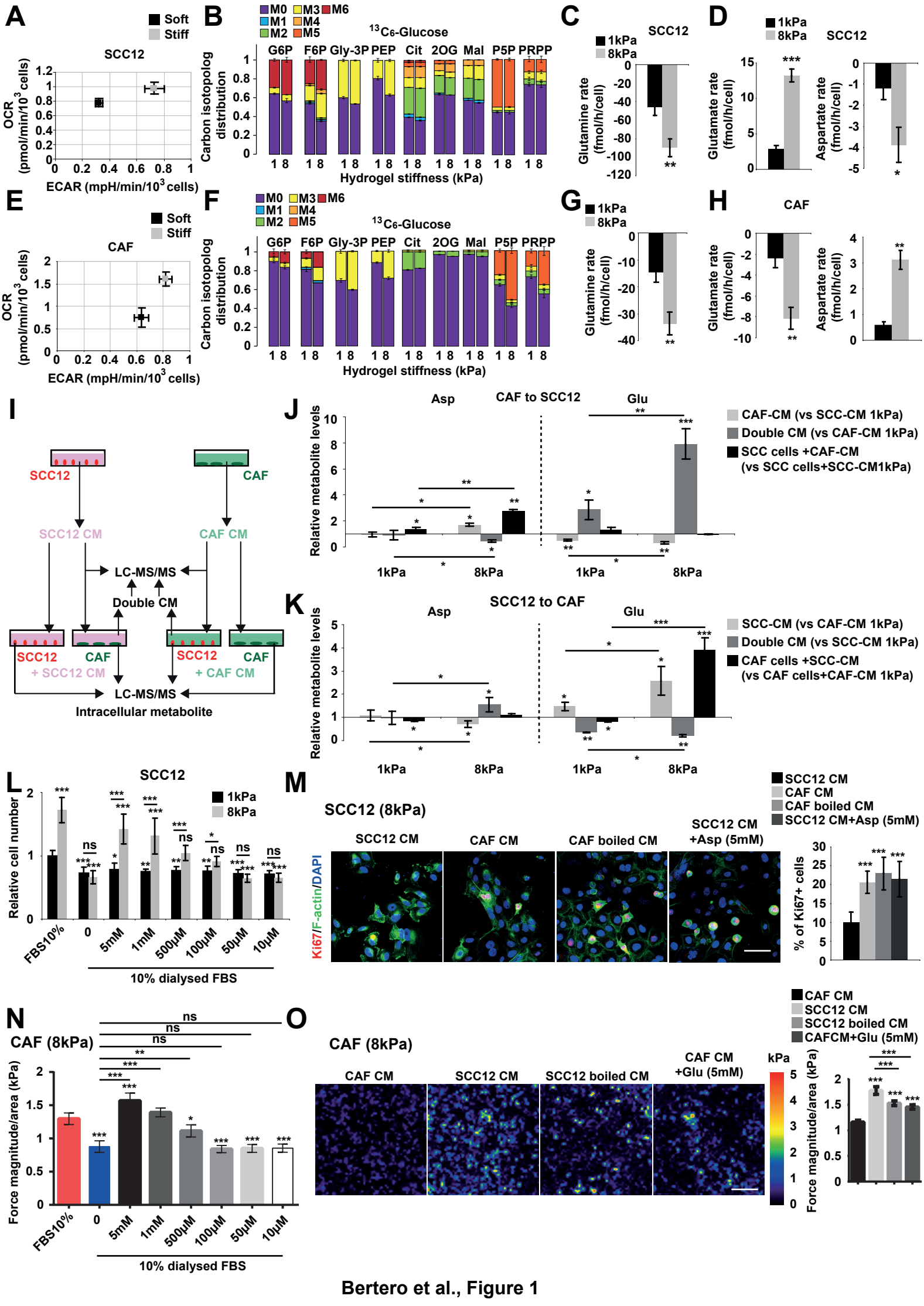

Bertero et al., Figure 1

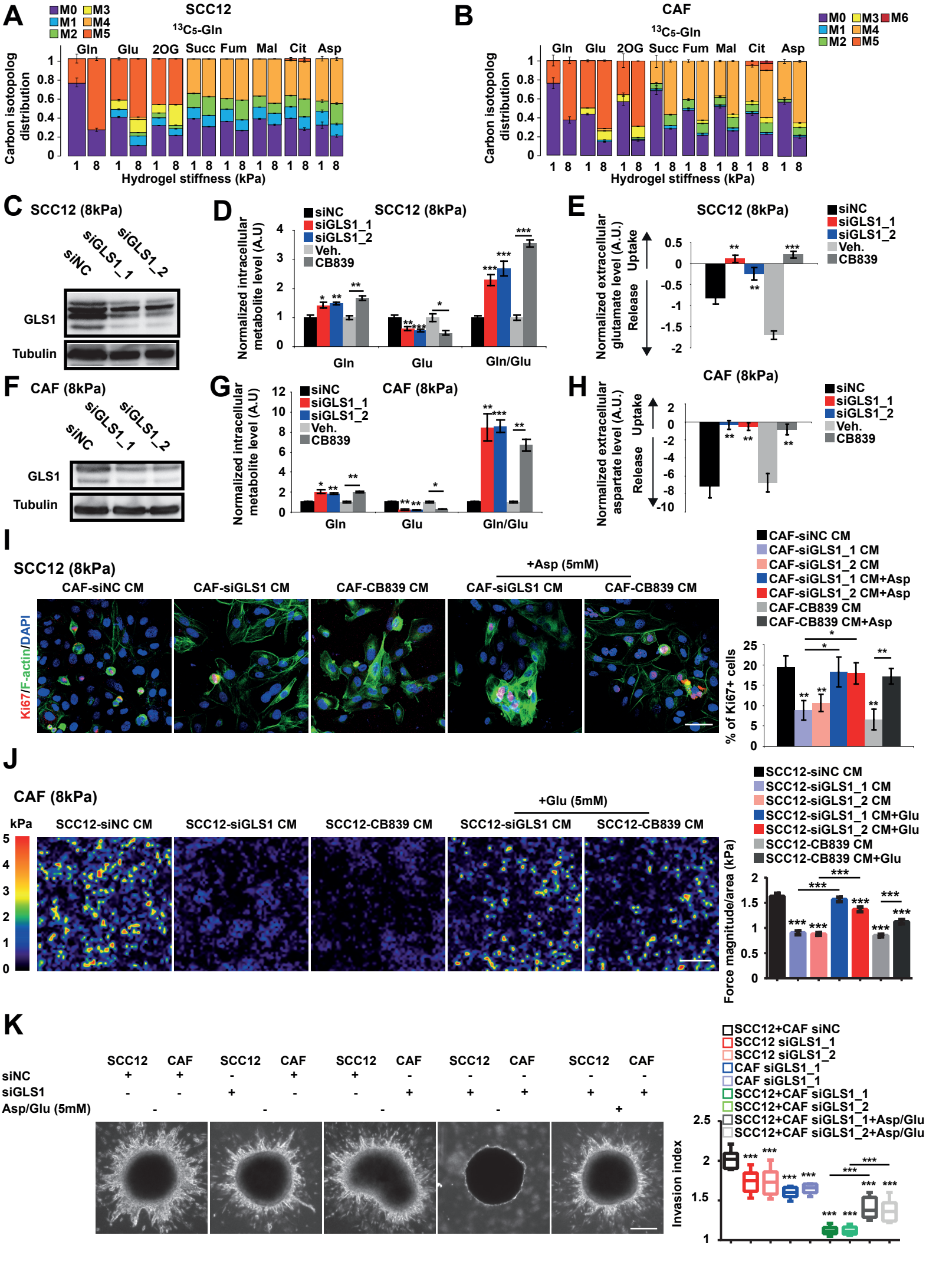

Bertero et al., Figure 2

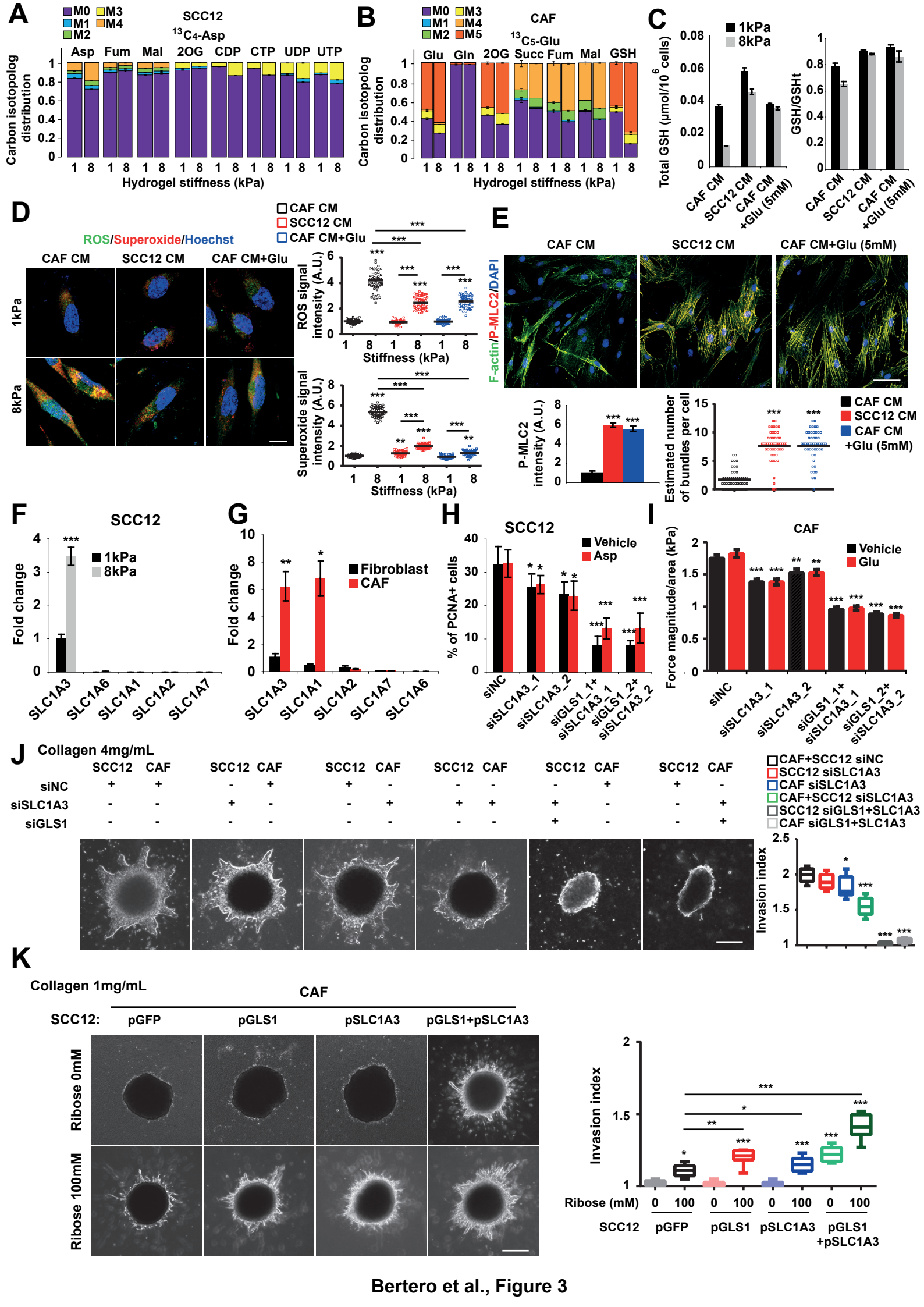

Bertero et al., Figure 3

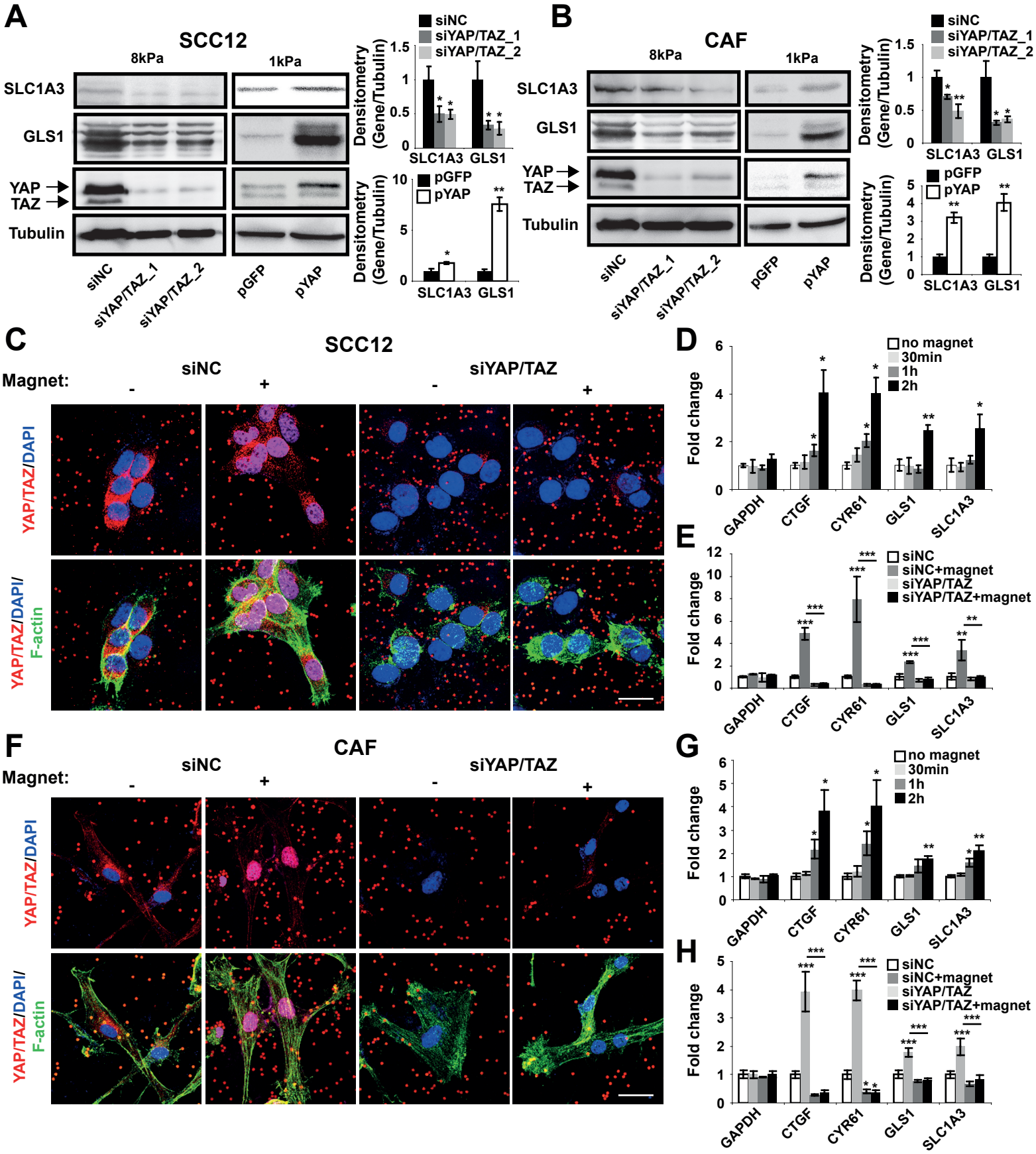

Bertero et al., Figure 4

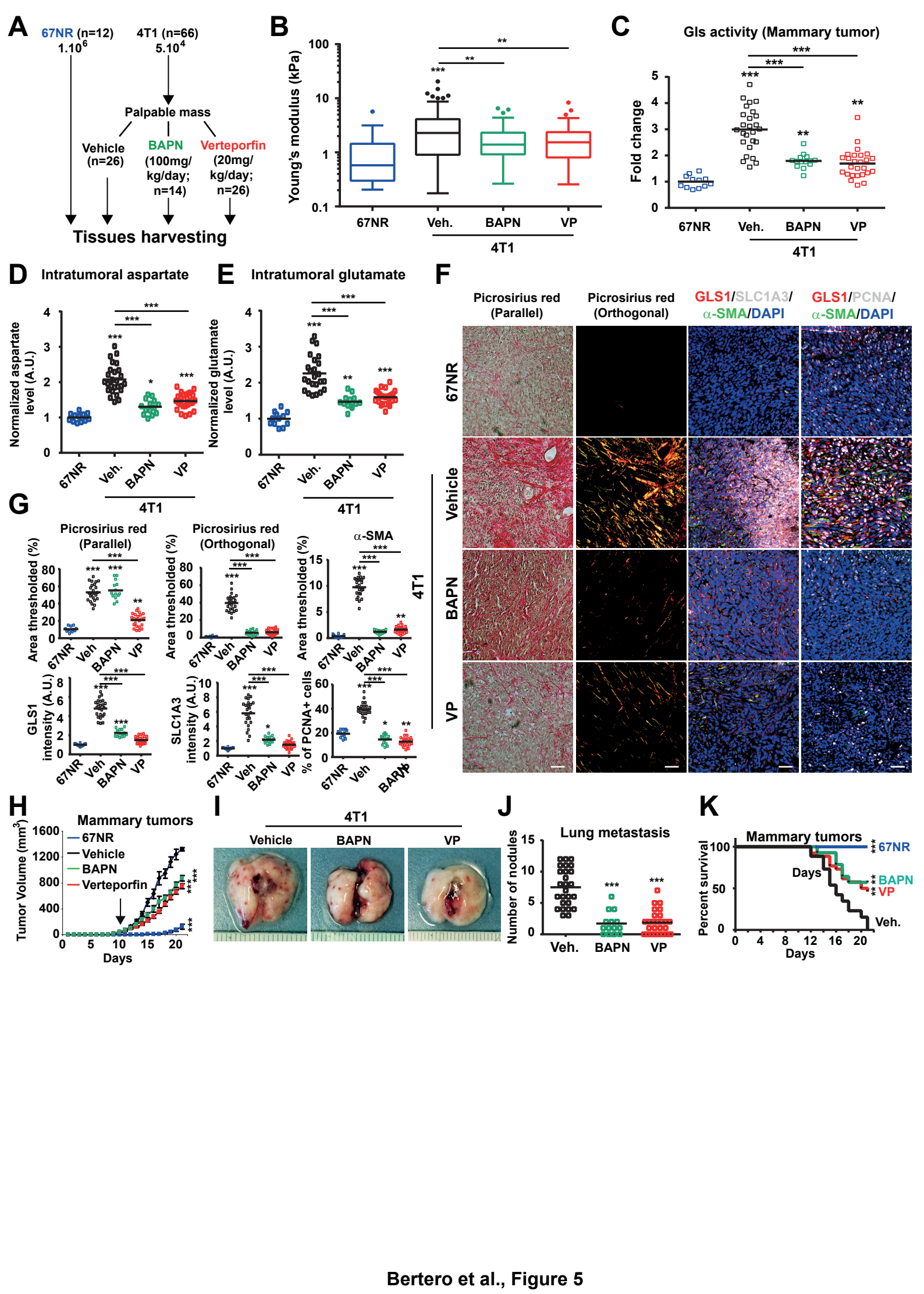

Bertero et al., Figure 5

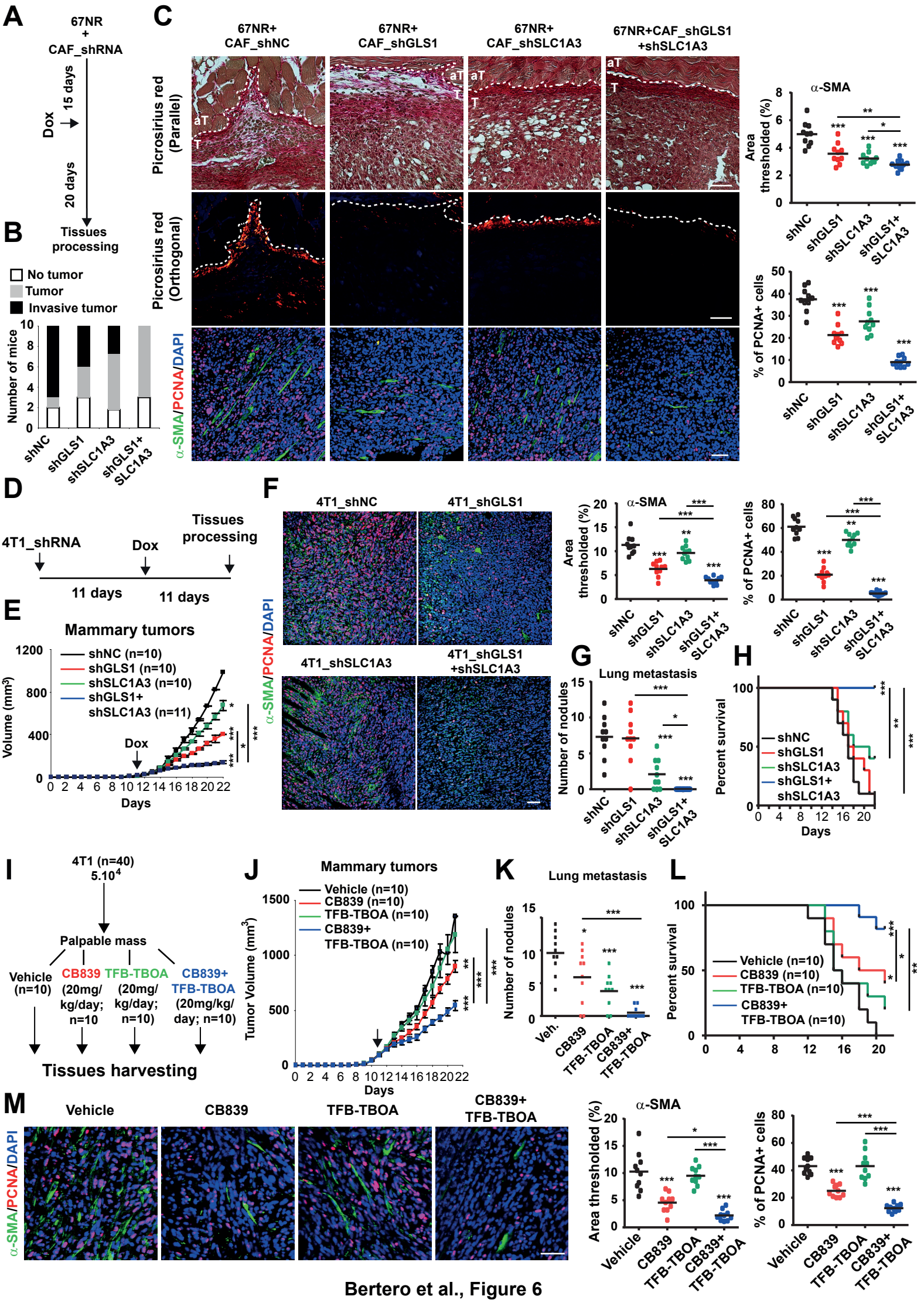

Bertero et al., Figure 6

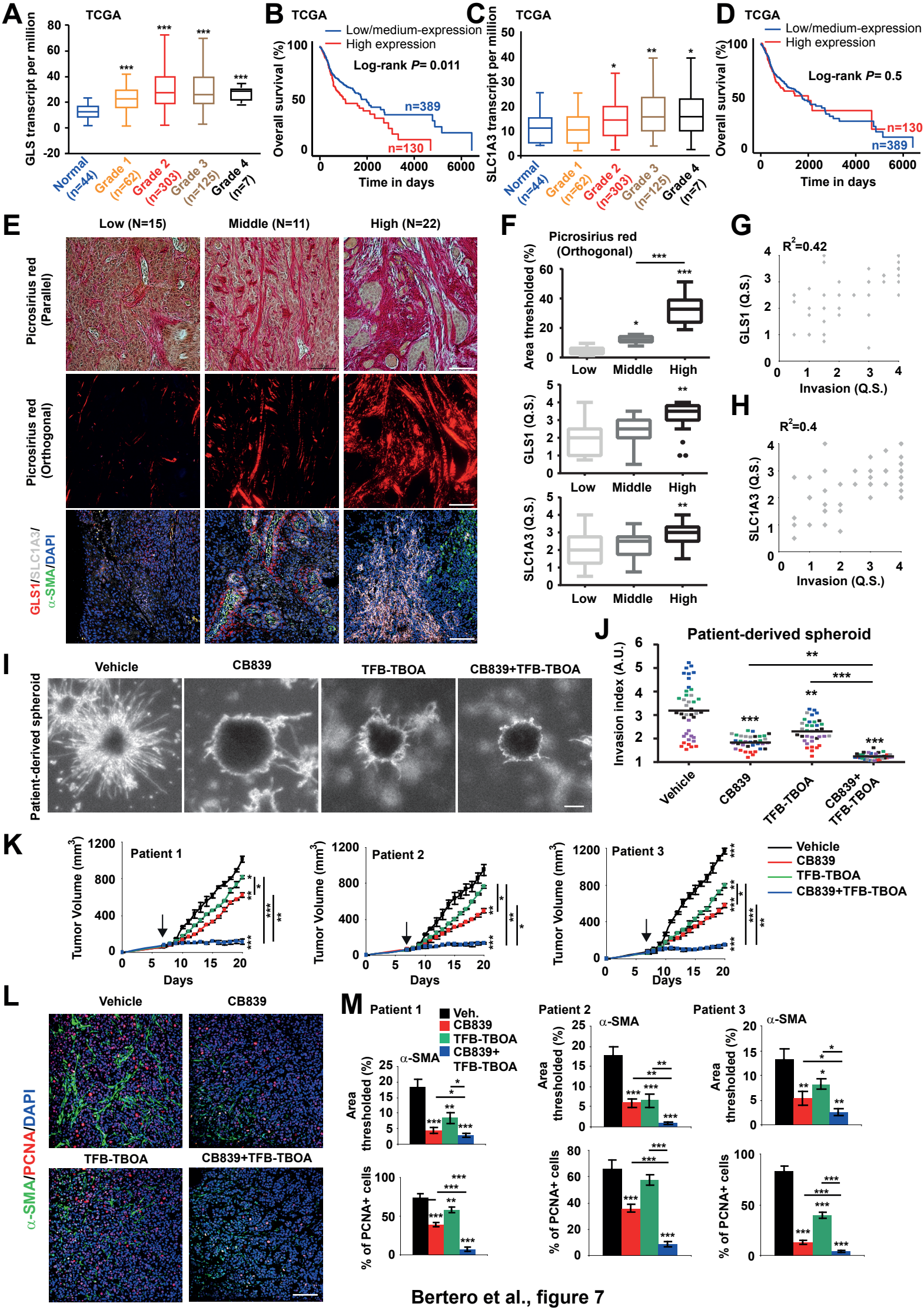

Bertero et al., figure 7

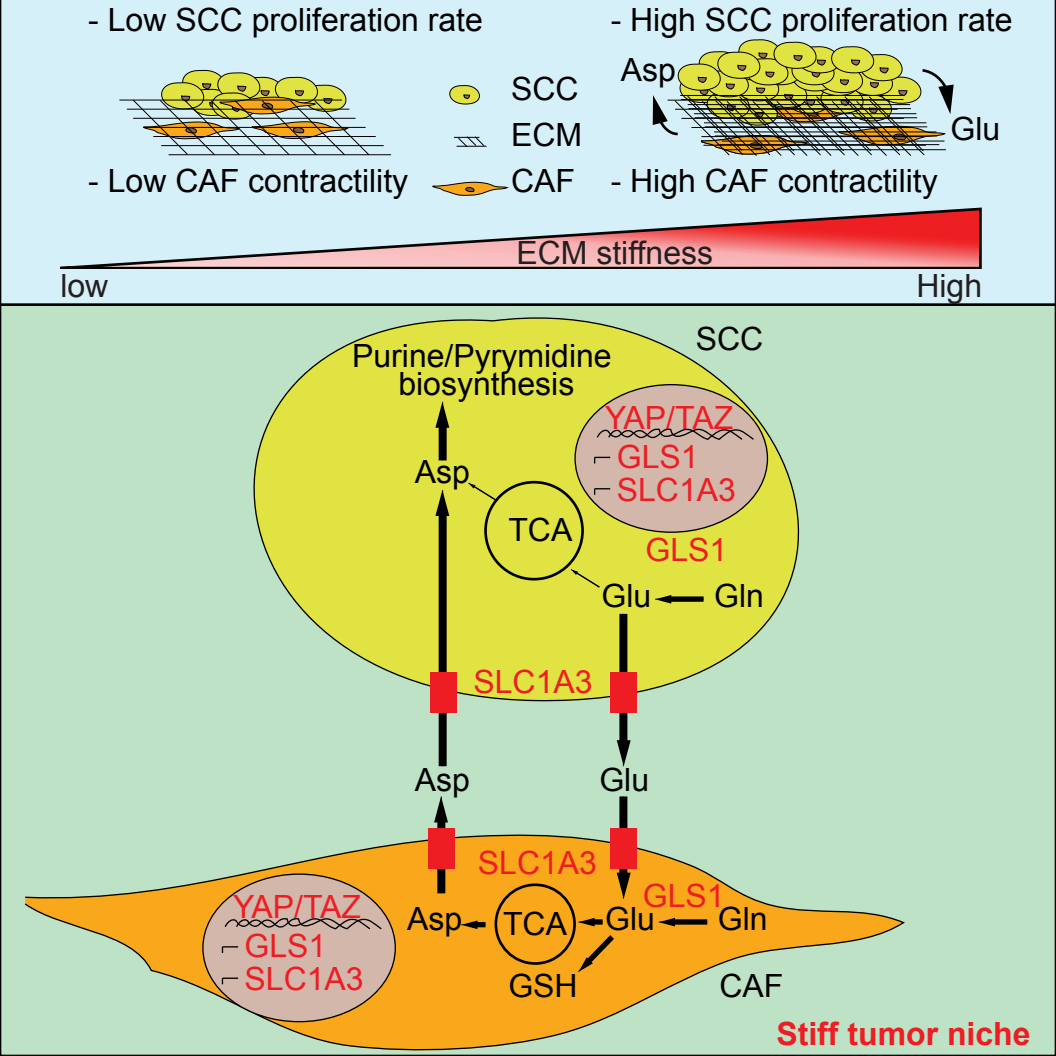
- Low SCC proliferation rate
- High SCC proliferation rate
Asp
Glu
SCC
ECM
CAF
- Low CAF contractility
- High CAF contractility
ECM stiffness
low
High
SCC
Purine/Pyrymidine biosynthesis
YAP/TAZ
GLS1
SLC1A3
Asp
TCA
GLS1
Glu
Gln
SLC1A3
Asp
Glu
SLC1A3
GLS1
YAP/TAZ
GLS1
SLC1A3
Asp
TCA
Glu
Gln
GSH
CAF
Stiff tumor niche